arXiv:astro-ph/0301401v2 30 Jan 2003

SiO Maser Survey toward the Inner Galactic Disk: $40^\circ \leq l \leq 70^\circ$ and $|b| \leq 10^\circ$

Jun-ichi NAKASHIMA[*]
Department of Astronomical Science, The Graduate University for Advanced Studies,
Nobeyama Radio Observatory, Minamimaki, Minamisaku, Nagano 384-1305
junichi@astro.uiuc.edu
and
Shuji DEGUCHI
Nobeyama Radio Observatory, National Astronomical Observatory,
Minamimaki, Minamisaku, Nagano 384-1305
deguchi@nro.nao.ac.jp

(Received 2001 July 24; accepted)

Abstract

We present the results of an SiO maser survey for color-selected IRAS sources in the area $40^\circ < l < 70^\circ$ and $|b| < 10^\circ$ in the SiO $J = 1$–0, $v = 1$ and 2 transitions ($\sim$ 43 GHz). We detected 134 out of 272 observed sources in SiO masers; 127 were new detections. A systematic difference in the detection rates between SiO and OH maser searches was found. Especially, in the color ranges with $\log(F_{25}/F_{12})$ smaller than -0.1, the detection rate of the SiO masers is significantly higher than that of OH masers. We found a possible kinematic influence of the galactic arm on the distribution of SiO maser sources. It was found that the velocity dispersion of SiO maser sources tends to decrease with the galactocentric distance. Using the present and previous data of SiO maser surveys, we found that the local velocity gradient of the rotational velocity of the Galaxy is consistent with the values obtained from other kinds of disk population stars within a statistical uncertainty. The Oort's constants, A and B, were computed from the gradient of the rotation curve for the present data, and were consistent with the IAU standard values. In addition, in order to check the reliability of IRAS positions, we observed toward the MSX positions for 5 MSX counterparts, which are located more than $20''$ away (but within $60''$) from IRAS positions. We detected all of these 5 sources in SiO masers.

Key words: Galaxy: kinematics and dynamics—masers—radio lines: molecular : circumstellar—star: late-type

---

[*] Present address: Department of Astronomy, University of Illinois at Urbana-Champaign, 1002 West Green

1. Introduction

OH/SiO masers from evolved stars have proven to be powerful tools for investigating stellar motion, even in optically obscured regions in the Galaxy (e.g., Lindqvist et al. 1992; Imai et al. 2002). Line profiles of OH masers usually show double-peak profiles (e.g., David et al. 1993). It has been well established that the middle velocity of the OH 1612 MHz double peaks gives the stellar velocity, where they are emitted from the approaching and receding parts of the circumstellar expanding shell (cf., Habing 1996). The radial velocity of the SiO maser emission from evolved stars usually falls in the middle of the OH 1612 MHz double peaks, giving the radial velocity of the central star to within a few km s^{-1} accuracy (Jewell et al. 1991). Up to now, large surveys in OH 1612 MHz have been made, and have covered almost all of the Galactic disk and bulge regions (e.g., te Lintel Hekkert et al. 1991; Chengalur et al. 1993; Blommaert et al. 1994; Sevenster et al. 1997). SiO maser surveys have also been made toward various regions of the Galaxy: bulge regions (Izumiura et al. 1994, 1995a, b), Galactic center regions (Imai et al. 2002; Miyazaki et al. 2001), outer-disk (Jiang et al. 1996) and high galactic latitude regions (Ita et al. 2001). In past SiO maser surveys, the Nobeyama 45-m telescope has played an important role because of its remarkable sensitivity at 43 GHz. As of today, however, an inner-disk region, $40^\circ < l < 70^\circ$, has never been surveyed in SiO masers at Nobeyama.

The inner-disk region provides a chance for us to tackle a couple of interesting themes, if it is surveyed systematically in SiO masers. First, one of the themes is a confirmation of the differences in the natures between OH/IR stars and IRAS/SiO sources. Although both of the OH/SiO masers are known to be indicators of O-rich stars (here, "O-rich" means a C/O ratio less than 1), the overlap of two masers is limited to only one third. This insignificance of the overlap suggests that IRAS/SiO sources should have different physical conditions compared with the OH/IR stars. A precise comparison from various viewpoints is needed to reveal the physical difference of these two objects. Because sensitive OH maser (1612MHz) surveys toward IRAS sources have been made with the Arecibo 300-m telescope in the inner-disk region (e.g., Lewis et al. 1990), we can make a minute comparison of the nature of OH/IR stars and IRAS/SiO sources using the result of SiO maser survey in the inner-disk region. Second, mass dependency of chemical evolution of evolved stars can be investigated in the inner-disk region. It has been suggested that O-rich AGB stars are predominantly located in the Galactic arms (e.g., Jiang, Hu 1993). This suggestion is attractive in terms of the chemical evolution of AGB stars. According to the dynamics of the Galaxy, AGB stars with a mass larger than 2–3 $M_\odot$ are preferentially found in the spiral arms. Therefore, if the concentration of O-rich star into the arms is real, massive AGB stars might prevent a chemical evolution from O-rich to C-rich stars, although the evolution from O-rich to C-rich star is a standard scheme of AGB evolution (here, "C-rich" means C/O ratio larger than 1). Because the spatial concentration of the O-rich AGB

Street, MC-221, Urbana, IL 61801

stars into the arms is relatively weak, a kinematical study is needed to confirm the affection from the arms. A tangential point of the Sagittarius–Carina arm is located at 5 kpc from the Sun in the inner-disk region; it is a quite appropriate distance to make a precise investigation of SiO maser sources in terms of the sensitivity of the Nobeyama 45-m telescope. (The tangential point means a point where a tangential line through the Sun contacts with the galactic arm.) Third, a local gradient of the rotation curve of the Galaxy is also an interesting theme to be investigated by an SiO maser survey in the inner-disk region. In the outer-disk region ($90^\circ < l < 230^\circ$), rotational velocities of O-rich AGB stars have been obtained based on the data of past SiO maser surveys (Jiang et al. 1996; Nakashima et al. 2000). On the other hand, the number of known SiO maser sources is quite limited in the inner-disk region, because of the absence of an SiO maser survey with the Nobeyama 45-m telescope. Therefore, the local inclination of the rotation curve of the Galaxy was never obtained through the motion of IRAS/SiO sources. Although the value has been obtained through a few kinds of disk population stars, a new value of the local inclination of the Galactic rotation curve through new kinds of disk populations would contribute to obtain more precise Galactic constants (e.g., Kerr, Lynden-Bell 1986).

In order to research the above issues, we systematically surveyed a sample of IRAS sources in the inner-disk region in SiO maser lines. In this paper, we report on the result of this systematic SiO maser survey. The outline of the paper is as follows. In section 2 we describe the observational details, results of observations, statistical characteristics of the data, and the reliability of the IRAS positions. In section 3 we give a statistical comparison with an OH maser survey and a kinematical analysis of the present data, and finally conclude the paper in section 4.

2. Observations and Results

2.1. SiO Maser Survey toward IRAS Sources

Simultaneous observations in SiO $J = 1$–0, $v = 1$ and 2 transitions at 43.122 and 42.821 GHz, respectively, were made with the 45-m radio telescope at Nobeyama during the period from 2000 April to 2001 March. The beam size of the telescope was about $40''$ at 43 GHz. In the present observation sessions, a cooled SIS receiver (S40) with a bandwidth of about 0.4 GHz was used, and the system temperature (including atmospheric noise) was about 200–300 K (SSB). The aperture efficiency of the telescope was about 0.57 at 43 GHz. The conversion factor from the antenna temperature to the flux density was 2.9 Jy K^{-1}. Acousto-optical spectrometer arrays of high and low resolutions (AOS-H and AOS-W) were used. The AOS-H spectrometer has 40 MHz bandwidth and 2048 frequency channels with an effective spectral resolution of 0.29 km s^{-1} at 43 GHz. Likewise, the AOS-W spectrometer has a 250 MHz bandwidth and 2048 frequency channels with an effective spectral resolution of 1.7 km s^{-1} at 43 GHz. We used multiple AOS-H spectrometers to cover a wide velocity range at a high frequency resolution.

Because line widths of masers are often less than 1 km s^{-1}, we needed the high resolution achieved by AOS-H. The radial-velocity coverage was ± 350 km s^{-1}. This velocity range was fully covered by the AOS-H spectrometers (AOS-W was used to confirm the detections). All of the observations were made by the position-switching mode using a $5'$ off position in the azimuth. The pointing of the telescope was checked every 2 or 3 hours by 5-point mapping of nearby SiO maser sources, V1111 Oph and χ Cyg. The pointing accuracy was usually found to be better than $10''$.

We selected a sample of observing sources in the Galactic plane area, $40^\circ < l < 70^\circ$ and $|b| < 10^\circ$, from the IRAS Point Source Catalog (Version 2, here after PSC). The distribution of the sources in the galactic coordinates is shown in figure 1. The source selection was made in terms of the IRAS 12 μm flux density, the IRAS colors and measurement quality flags. The criteria of the selection are as follows:

1. $F_{12} > 3$ Jy,
2. $-0.2 < C_{12} \equiv \log(F_{25}/F_{12}) < 0.2$,
3. $C_{23} \equiv \log(F_{60}/F_{25}) < -0.5$,
4. $Q_{12} = Q_{25} = 3$,

where F_{12}, F_{25}, and F_{60} are the IRAS 12, 25 and 60 μm flux densities, Q_{12} and Q_{25} are the measurement quality flags for 12 and 25 μm, respectively, and "3" means the highest quality. These selection criteria effectively extract dust-enshrouded objects with $T_{\rm dust} \simeq 240$–450 K from the IRAS PSC. It was found in past SiO maser surveys that the detection rate of SiO masers is maximized at an IRAS color, $C_{12} \simeq 0$ ($T_{\rm dust} \simeq 300$ K) and that the rate drops quickly in $|C_{12}| > 0.2$ (e.g., Jiang et al. 1995; Nyman et al. 1998). Therefore, we centered the color of $C_{12} = 0.0$ in the criterion 2 to maximize the detection rate. Finally, 340 sources were selected from IRAS PSC by above criteria, and 272 have been observed. Almost all of the samples above $F_{12} = 8$ Jy were observed (more than 99%). In the case of faint sources with $F_{12} < 8$ Jy, the completeness of the survey is somewhat low (mentioned later).

Raw data were processed by flagging out bad scans, making r.m.s.-weighted integrations, and removing the slope in the baseline. The detections of maser lines were judged by the following criteria. For narrow spike-type emissions, the peak antenna temperature must be greater than the 3 σ level of the r.m.s. noise. For broad and multiple spiky emissions, the effective signal-to-noise ratio (S/N) over the line width must be larger than 5; the effective S/N is calculated from integrated intensities within maximum line width (about 15 km s^{-1} in typical cases) and the rms noise. In addition, we carefully inspected each spectrum by eye and discarded some spurious emissions and marginal detections that satisfy the above criteria.

As a result of the present observation, we detected 134 out of 272 observed sources in either SiO $J = 1$–0, $v = 1$ or 2 transitions; 127 of 134 detected sources were newly detected objects in SiO masers. The observational results are summarized in table 1 for the detected sources and in table 2 for the non-detected sources. The spectra of the detected sources are shown in figure 2. Velocities, V_{lsr}, given in table 1 are radial velocities at an intensity peak in the spectra, except for the case of IRAS 19229+1708. The intensity-weighted radial velocity normally coincides with the velocity at the peak within a few km s^{-1} (Jewell et al. 1991). IRAS 19229+1708 exhibits an extreme broad line-width with triple peaks. In addition, the intensity peak of the $v = 1$ line of IRAS 19229+1708 is clearly shifted from its systemic velocity according to the profile of $v = 2$ line. Therefore, we adopted an intensity weighted mean of radial velocity as a systemic velocity for IRAS 19229+1708. Finally, the detection rate was 49%. The detection rates in the ranges of $40^\circ < l < 50^\circ$, $50^\circ < l < 60^\circ$, $60^\circ < l < 70^\circ$ are 61%, 47% and 38%, respectively. This variation of the detection rate with galactic longitude can be seen in figure 1.

(Figure 1 here)
(Figure 2 here)
(Table 1 here)
(Table 2 here)

2.2. Position Confirmation Using the MSX Catalog

It has been believed that the uncertainties of the source positions in the IRAS PSC are within about $10''$ (Beichman et al. 1988; Jiang et al. 1997). This position uncertainty, if it is reliable, is sufficiently accurate for observations by the Nobeyama 45-m telescope, because of its half-power beam width of $40''$ at 43 GHz. Recently, however, Deguchi et al. (2001) found a non-negligible number of near-infrared counterparts of IRAS sources at positions separated from its IRAS positions by more than $20''$. Because an observing region in Deguchi et al. (2001) is close to the galactic center, it seems that the main reasons for the position uncertainty of IRAS PSC are congestion of sources and a large beam of an infrared detector of IRAS. On the contrary, the sources in the present surveyed region were not very crowded compared with the region researched by Deguchi et al. (2001), and the IRAS positions would be relatively reliable than the Deguchi et al. (2001)'s case. Here, however, to make sure of the reliability of the source positions of the present sample, we compared the IRAS positions of SiO non-detections with MSX positions (MSX: Midcourse Space Experiment; Price et al. 1997). Because the typical uncertainty of astrometric positions in the MSX catalog is a few arcseconds, the reliability of the IRAS positions could be checked by cross checking with the MSX positions. As a consequence, we found that 5 IRAS sources with SiO non-detection separate from the MSX positions by more than $20''$ (but within $60''$). In table 3, the separations between the IRAS position and the MSX position, C-band (centered at 12.13 μm) and E-band (centered at 21.34 μm) intensities in the MSX catalog, and IRAS 12 and 25 μm flux densities of these 5 IRAS sources are shown. The MSX flux densities are approximately proportional to the IRAS

flux densities, though some scatter is seen. The scatter would be due to the pulsation of AGB stars. We observed these 5 sources once again at their MSX positions, and were detected in SiO masers for all 5 sources. The results of these additional observations are summarized in table 4, and the spectra of the SiO masers are shown in figure 3. In order to maintain consistency with previous SiO maser surveys made at Nobeyama, above 5 detections at the MSX positions were excluded in the statistical analysis discussed in the following sections, because the IRAS positions were used as the observing positions in previous SiO maser surveys. However, in the present research, the number of sources with a large position uncertainty of more than $20''$ was only 5 in 138 nondetections, which would be negligible in the statistics.
(Figure 3 here)
(Table 3 here)
(Table 4 here)

2.3. *Statistical Characteristics*

In the present work, we extended the survey latitude up to $|b| = 10^\circ$ ($|b| < 3^\circ$ in previous works, cf. Izumiura et al. 1999; Deguchi et al. 2000a, b). Therefore, we checked the variation in the detection rate with the galactic latitude. The detection rates were 47% in the range of $|b| < 3^\circ$ and 52% in the range of $3^\circ < |b| < 10^\circ$. No remarkable difference could be seen between these two values. The detection rate of SiO masers, 49%, in the present survey suggests a decreasing tendency of the detection rate with the galactic longitude. This tendency is consistent with the results in previous SiO maser surveys toward the inner galactic area (Izumiura et al. 1999; Deguchi et al. 2000a, b; Nakashima et al. 2002; Jiang et al. 1996). However, we have to be cautious of concerning this result, because of the difference in the color selection criteria of each sample. In previous SiO maser surveys towards the inner bulge (Izumiura et al. 1999; Deguchi et al. 2000a, b), the color range, $0.0 < C_{12} < 0.1$, was used as a source selection criterion. In every 10°-step sub-samples from $l = 40^\circ$ in the longitude, the detection rates in the color range, $0.0 < C_{12} < 0.1$, are 44% ($40^\circ < l < 50^\circ$), 40% ($50^\circ < l < 60^\circ$), and 31% ($60^\circ < l < 70^\circ$), respectively, in the present survey; the average detection rate was 42%. In fact, detection rates in previous surveys were 56% for the bulge bar ($15^\circ < l < 25^\circ$, $|b| < 3^\circ$; Izumiura et al. 1999), 49% for the inner galactic bulge ($|l| < 3^\circ$, $|b| < 3^\circ$; Deguchi et al. 2000aa), 62% for the outer galactic bulge ($-10^\circ < l < 25^\circ$, $|b| < 3^\circ$; Deguchi et al. 2000bb), and 48% for the inner galactic disk ($25^\circ < l < 40^\circ$, $|b| < 3^\circ$; Nakashima et al. 2002). The present detection rate is less than the values obtained in the inner Galaxy surveys. This clearly confirms the decreasing tendency of the detection rate with the galactic longitude. The detection rate in the outer galactic disk ($90^\circ \leqq l < 230^\circ$, $|b| < 10^o$), which is limited in the sample with the color, $0.0 < C_{12} < 0.1$, was 0% (14 sources were observed). The detection rate obtained in the present work lies between the two detection rates of the outer- and inner-disk surveys, supporting a monotonous decrease of the detection rate with the galactic longitude. All of the SiO surveys mentioned here were made using the same telescope (Nobeyama 45-m telescope), receiver (S40), and observation mode (position-switching). In addition, the average integration times per one object were almost same (about 10 min on source) in all surveys. Therefore, the sensitivities can be considered to be sufficiently similar to compare the detection rates.

2.4. IRAS Characteristics of the Sample

Figure 4 shows a histogram of the IRAS 12 μm flux densities and the variation of the detection rate with the IRAS 12 μm flux density in the present sample. The detection rate tends to increase with the 12 μm flux density. In ranges of $20 < F_{12} < 24$ Jy and $F_{12} < 4$ Jy, the detection rates tend to be slightly higher and lower, respectively, than those of the other ranges. In $20 < F_{12} < 24$ Jy, because the number of samples is extremely few, the rise may be a statistical fluctuation. On the other hand, in $F_{12} < 4$ Jy, because the number of samples in this range is more than 25, it can not be disregarded. In fact, this kind of decline in the detection rate has been seen in previous SiO maser surveys (e.g. Deguchi et al. 2000bb; Izumiura et al. 1999).

Generally speaking, the intensity of SiO maser lines tends to increase with the IRAS 12 μm flux density. For instance, in the case of the NRO 45-m telescope, the expected antenna temperature of the SiO maser line from IRAS PSC source with $F_{12} = 4$ Jy is approximately 0.2 K. Because of the time variation, the intensity of a maser line varies by a factor of about 10. Therefore, the antenna temperature of the SiO maser line from the IRAS PSC sources with $F_{12} = 4$ Jy is expected to lie between about 0.04 and 0.4 K. The r.m.s. level of the present survey data was 0.05 K on average. In the present work, we used the 3 σ level as a border of detection (for narrow lines; most of detections falls in this case). The 3 σ level corresponds to 0.15 K in the antenna temperature. Hence, it is possible that nearly half of the potential SiO detections in the range of $3 < F_{12} < 4$ Jy are missed in the present survey. If we made exposures for a longer time than in the present case, the detection rate could be increased up to about 40% in the range of $3 < F_{12} < 4$ Jy according to the detection rates in other intensity ranges.

Figure 5 shows the two-color (left) and C_{23}–b (right) diagrams for the present sample. The SiO detection rates were 68%, 52%, 50% and 30% in the C_{23} ranges of $-0.9 < C_{23} < -0.8$, $-0.8 < C_{23} < -0.7$, $-0.7 < C_{23} < -0.6$, and $-0.6 < C_{23} < -0.5$, respectively. In general, carbon stars in the two-color diagram distribute at the upper part of O-rich stars (van der Veen, Habing 1990). The present sample involves three previously known carbon stars (IRAS 19029+0808, IRAS 19238+1159, IRAS 19304+2529, Jura, Kleinmann 1990; Volk et al. 1992), as indicated in the left panel by the large crosses. The three carbon stars distribute at the uppermost part in the left panel. This fact supports that the rate of carbon stars in the sample tends to increase with an increase of the color C_{23}.

In the case of the previous SiO maser surveys towards inner-disk/bulge regions, C_{23}–b

diagram showed an arch-like structure at the bottom (the peak of the arch is at $b = 0°$), indicating a strong reddening in the Galactic plane (e.g. Figure 4 of Deguchi et al. 2000bb). On the contrary, such a structure cannot be seen in the b–C_{23} diagram in the present sample. This would suggest that the contamination by the interstellar dust in the C_{23} color is not strong in the present sample, although the present criteria of source selection is slightly different from those in previous surveys.

(Figure 4 here)
(Figure 5 here)

2.5. Comparison with OH Data

Figure 6 shows a histogram of the color, C_{12}, for the observed sources. The number of sources surveyed in both SiO and OH masers was 240 (in 272 sources), and the number of sources, which were detected in both of SiO and OH masers, was 75. Mainly, OH maser surveys were made with the Arecibo 300-m telescope (about 95% of OH observations in table 5 were made at Arecibo). Owing to the large aperture of the Arecibo 300-m telescope, the OH maser survey was made deeper than the present SiO maser survey. The shaded portions show the numbers of SiO and OH detections. The solid and dotted lines (line graph) show the detection rates of the present SiO maser survey and the OH maser survey.

The main characteristic in figure 6 is a difference of the two line graphs. The detection rate of the SiO maser is roughly constant through all of the color ranges. On the other hand, the detection rate of the OH maser tends to increase with the color. The present survey is somewhat incomplete for sources with $F_{12} < 4$ Jy. However, the above tendency does not change even if the sources with $F_{12} < 4$ Jy are excluded. This difference of the detection rates between the OH and SiO masers implies that evolved AGB stars with a thick circumstellar envelope tend to exhibit OH masers more often than SiO masers, though AGB stars with a thin circumstellar envelope tend to exhibit SiO masers more than OH masers. However, large ($\gtrsim$ 80%) OH detection rate may be due to poor statistics at $C_{12} > 0.1$.

We should thus note any difference in the variability of OH/SiO masers. In this kind of survey, the detection rate of SiO masers always gives a lower limit for the true probability for the appearance of SiO masers because of their strong variability. Whereas OH masers are relatively stable compared to SiO, they are also variable. If we make additional surveys for non-detections in SiO, the detection rate would increase in some measure. This fact supports the higher detection rate of SiO than that of OH in the bluer color range in figure 6. The IRAS color, C_{12}, has been believed to be an evolutional indicator of AGB stars. The value of C_{12} tends to increase with the evolution of AGB stars (e.g., van der Veen, Habing 1988). In this sense, OH masers tend to be appendant in more evolved objects than SiO masers.

(Figure 6 here)
(Table 5 here)

3. Discussion

3.1. Luminosity Distance

The distance is calculated from the bolometric flux of the sources, which is computed from the IRAS 12 μm flux density, F_{12}, and a bolometric correction for O-rich stars (van der Veen, Breukers 1989). In the present work, we assumed that the luminosity of the AGB star is 8000 $L_\odot$; this corresponds to the luminosity of a star with mass of $\sim 2\ M_\odot$ near to the tip of the AGB in the models of Vassiliadis, Wood (1993). Details of the distance calculation can be found in our previous papers (e.g., Nakashima et al. 2000). The obtained distances are given in table 5. The luminosity distance involves an uncertainty of about 20–30%, which is partly due to the uncertainty of the luminosity assumption of 8000 $L_\odot$, and partly due to the light variation of AGB stars. In fact, a non-negligible number of color-selected AGB star candidates are mira-type variables (e.g., Nakashima et al. 2000). In the case of short-period miras with $P \lesssim 400$ d, if we know the pulsation period of the star, their distances can be obtained with higher accuracy using the period-luminosity relation (e.g., Nakashima et al. 2000).

3.2. Kinematical Characteristics of the Sample

Figure 7 shows $V_{\rm lsr}$ versus the luminosity distance (D_L) for 134 SiO detected sources. Sources above and below $l = 50°$ are classified by open and filled circles, respectively. The solid and broken curves are radial velocities expected from the circular motion and the flat rotation curve on the directions $l = 40°$ and 70° (see the caption of figure 7 for the details of the flat rotation curve). These two curves gradually separate from each other with the distance. Therefore, if the motion of SiO maser sources follows the galactic rotation (circular motion and flat rotation curve), the open circles ($l < 50°$) in figure 7 should distribute in a relatively higher velocity range than the open circles ($l > 50°$). Actually, we can see the difference in the two distribution of the open and filled circles in Figure 7.

(Figure 7 here)

Figure 8 shows the l–$V_{\rm lsr}$ diagram for SiO detected sources overlaid on the CO $J = 1$–0 line map (taken from Dame et al. 1987). In figure 8, the distribution of the present data is almost the same as that of CO line; this suggests that the present survey reaches to the tangential point. The $V_{\rm lsr}$ distribution of SiO maser sources is relatively wider than the extent of the CO map. This difference in the $V_{\rm lsr}$ distribution would originate mainly in the difference of the velocity dispersions between CO clouds and SiO maser sources.

A moderate concentration of sources can be seen in the area, $l \simeq 40°$–$53°$ and $V_{\rm lsr} \simeq 30$ km s^{-1}–60 km s^{-1}. Taylor, Cordes (1993) pointed out in a study of the distribution of free electrons that the tangential point of the Sagittarius–Carina arm exists at a distance 4–8 kpc from the Sun on the direction of $l = 45°$. Therefore, it is possible that this weak concentration of sources originates from the Sagittarius–Carina arm (though it is not so clear). A similar weak concentration of sources, possibly due to the Scutum–Crux arm, was also reported in Nakashima et al. (2002).

We can see a source-deficient region (roughly surrounded by the dotted ellipse in figure 8). In order to confirm this deficiency, we applied the Kolmogorov–Smirnov (K–S) test (Chakravarti et al. 1967) for three subsets of the SiO detections divided by the galactic longitude: group A ($40° < l < 45°$), group B ($45° < l < 50°$), and group C ($50° < l < 55°$). The source-deficient region mentioned above is mainly included in group B. The cumulative probability distributions for the three groups are shown in figure 9. The maximum difference in the cumulative probability (D value) between groups A and B, groups B and C, groups C and A are 0.21, 0.24, and 0.13, respectively. The values of D_α, which provide a boundary to judge at the 99% confidence level whether the difference of two distributions is reliable, are 0.15, 0.13, and 0.15 for pairs of groups A and B, groups B and C, groups C and A, respectively. According to the D and D_α values, the difference in the distribution along the perpendicular axis in figure 9 is significant with more than a 99% confidence level between groups A and B and groups B and C, but not between groups A and C. In this statistical treatment with K–S test, we assumed that the sampling condition was unity around the source–deficient region. The maximum different points in the cumulative probability diagram between groups A and B and between groups B and C lie just at the source-deficient region. Based on these results, we conclude that the source-deficient region surely exists on the l–v diagram.

(Figure 8 here)
(Figure 9 here)

3.3. Variation in the Velocity Dispersion

We divided the detected sources into three groups based on the galactocentric distance: I ($R < 6.5$ kpc, 25 sources), II ($6.5 \leqq R < 7.5$ kpc, 64 sources), and III ($R \geqq 7.5$ kpc, 44 sources). Then, the velocity dispersion (root mean square of the residues, which is the result of subtracting the circular and solar motions from $V_{\rm lsr}$) was calculated for three groups. Here, we assumed that the circular orbit and flat rotation curve as the galactic rotation (see the caption of figure 7 in detail), and that the galactocentric distance of the Sun is 8.5 kpc. The calculated velocity dispersions are 35.2 (+8.2, −5.2) km s^{-1}, 32.2 (+4.3, −3.2) km s^{-1}, and

30.6 (+5.1, −3.6) km s^{-1} for groups I, II, and III, respectively. The values in parenthesis are the 80% confidence intervals. It seems that the velocity dispersion tends to decrease with the galactocentric distance. In order to confirm this tendency from a statistical viewpoint, an F-test was made. The confidence level of the difference in the dispersion between the nearest group I ($R < 6.5$ kpc) and the furthest group III ($R \geqq 7.5$ kpc) is 79%. According to the results from the F-test, we cannot rule out a possibility for the increasing tendency of the velocity dispersion with the galactic radius, though the statistical confidence level is somewhat low. It should be noted that the velocity dispersions obtained here are a somewhat weighted mean of the radial and tangential dispersions, with a higher weight to the tangential one. This effect is most significant in group III. In addition, the velocity dispersion obtained here is similar to that for M-type stars in the solar neighborhood (e.g., Dehnen, Binney 1998; Mihalas, Binney 1981).

3.4. Influence of Arms on the SiO Maser Source Distribution

In the previous subsection 3.2, although we found that the weak concentration of SiO sources in the l–V_{lsr} diagram (figure 8) is possibly due to the spiral arm, it was not so clear. In order to confirm the spatial distribution of the present sample, the positions of the present sample projected onto the galactic plane are shown in figure 10. A spiral model, which is indicated as the background in figure 10, is referred from Taylor, Cordes (1993). In figure 10, the IRAS sources in the present sample ($F_{12} > 3$) for which observations were not made are also plotted with small dots. In addition, faint sources with $F_{12} = 1$–3 Jy, which have the same colors as those in the present sample, are plotted with small crosses. Because the present survey is incomplete for faint sources with $F_{12} < 3$ Jy, the distribution of the observed sources is inhomogeneous in a distant region over 6 kpc from the Sun. On the contrary, the distribution of the observed sources in the nearby region within 6 kpc is relatively homogeneous because of the completeness of the present survey for bright sources with $F_{12} > 3$ Jy.

Although the distribution of all samples is almost homogenous, except for the distant region, the individual distributions of open/filled circles are systematically different from each other in figure 10. Specifically speaking, the number density of the filled circles tends to increase with a decrease of the galactic longitude. It is difficult to say based only on the present data that this tendency originates from the influence of the galactic arm, but we should note that the tangential point of the Sagittarius–Carina arm exist in the direction of $l \sim 40^\circ$, where the number density of filled circles (SiO detections) is maximized. Jiang, Hu (1993) suggested that the spatial distribution of O-rich AGB stars shows a similar spiral structure as that presented by Georgelin et al. (1976). Fitting with the spiral structure of Georgelin et al. (1976), Jiang, Hu (1993) derived that the average luminosity of the objects in the sample is 8300 $L_\odot$; this value is appropriate as a luminosity of an O-rich AGB star (e.g., Vassiliadis, Wood 1993). This tendency is attractive for studying the chemical evolution of AGB stars, especially with a massive main-sequence mass larger than 3 $M_\odot$. According to the dynamics of the Galaxy, AGB stars with masses larger than $\sim 3\ M_\odot$ are preferentially found in the spiral arms (Jiang, Hu 1993). From the concentration of SiO masers, if it is real, most SiO maser sources in the concentration might be O-rich massive AGB stars with the main-sequence mass being larger than $M_{\rm ms} \sim 3\ M_\odot$. This agrees with the current stellar evolution models based on Hot Bottom Burning (nuclear processing of carbon into oxygen and nitrogen at the base of the convective mantle for the most massive AGB stars; Iben, Renzini 1983; Wood et al. 1983). Ventura et al. (1999) show that stars with $M_{\rm ms} > 3.8\ M_\odot$ always keep the O-rich chemistry through their evolution, although AGB stars with $\mathrm{M}_{ms} < 3.8\ \mathrm{M}_\odot$ evolve from an O-rich star to a C-rich star. In fact, the higher mass limit for carbon stars in the LMC is currently believed to be $\sim 4\ M_\odot$ (Groenewegen, de Jong 1993; Marvel, Boboltz 1999). In order to clarify whether the concentration of SiO masers into the arms is real or not, we need more accurate information about the distance. Fortunately, in the near future, distances to SiO masers will be directly determined by measuring the annual parallax using Japanese differential VLBI network, VERA (Honma et al. 2000).

(Figure 10 here)

3.5. Rotation Curve

Figure 11 is a plot of the rotational velocity of SiO sources against the galactocentoric distance. The rotational velocity was calculated from the radial velocities by subtracting the rotational velocity (220 km s^{-1}) of the local standard of rest, while assuming that the radial velocity is a projection of the circular rotational velocity along the line of sight. The solid line shows the running mean of $V_{\rm lsr}$ in every 1 kpc width with 0.5 kpc steps from 5.5 kpc to 11 kpc. The dotted line shows the best fit line to the data. In the calculation, we added the data in Jiang et al. (1996) in the outer-disk; the selection criteria of the sample and the method to obtain distances in Jiang et al. (1996) are the same as those used in the present work. The least square method gives the best fit,

$$V_{\rm rot} = 202.2(\pm 14.24)\,[\mathrm{km\,s^{-1}}] - 4.8(\pm 1.7)\,[\mathrm{km\,s^{-1}kpc^{-1}}] \times (R - R_0)[\mathrm{kpc}], \qquad (1)$$

where R_0 is assumed to be 8.5 kpc. The obtained inclination is consistent with the values obtained for the other kind of disk population stars [-2.1 ± 2.4 km s^{-1} kpc^{-1} for OB stars, -5.7 ± 3.2 km s^{-1} kpc^{-1} for Cepheid (e.g. Frink et al. 1996)] within a statistical uncertainty. Oort's constants estimated from this inclination are $A = 15.4 \pm 0.9$ km s^{-1} kpc^{-1} and $B = -10.5 \pm 0.9$ km s^{-1} kpc^{-1}. These values are close to the IAU standard values ($A = 15$ km s^{-1} kpc^{-1}, $B = -10$ km s^{-1} kpc^{-1}; Kerr, Lynden-Bell 1986). The value of 202.2 km s^{-1} for the rotation velocity at the solar circle is quite similar to those derived from motion of the HI gas component by Merrifield (1992) and Honma, Sofue (1997). According to the present results, the bulk motion of the SiO maser sources in the solar neighborhood would be the same as that of the other disk population stars and the gas component.

In recent works on the kinematics of SiO maser sources in the outer-disk, the obtained inclinations of the rotation curve, which were limited to the range of $R = 8.5$–11.5 kpc, were -21.7 ± 5.7 km s^{-1} kpc^{-1} (Jiang et al. 1996), and -15.4 ± 7.7 km s^{-1} kpc^{-1} (Nakashima et al. 2000). These values are somewhat steeper than the present results, indicating that the rotational velocity of the Galaxy tends to decrease in the outer region further than the Sun; this result is consistent with observations of the other kind of disk population stars (Frink et al. 1996).

(Figure 11 here)

4. Conclusion

We observed 272 color-selected IRAS sources in the galactic disk area, $40^\circ < l < 70^\circ$ and $|b| < 10^\circ$, in the SiO $J = 1$–0, $v = 1$ and 2 transitions, and detected 134 in SiO masers; 127 were new detections in SiO masers. The main results of this research are as follows:

1. A systematic difference in the detection rates between SiO and OH maser searches was found. In the ranges below $C_{12} = -0.1$, the SiO detection rate is higher than the OH detection rate.
2. Possible concentrations of SiO sources in the $l - V_{\rm lsr}$ diagram and in the face-on view diagram might be attributed to the spiral arm (Sagittarius–Carina arm). The observed sources with SiO masers moderately concentrate into the tangential point of the Sagittarius–Carina arm in the spatial distribution.
3. The velocity dispersion of SiO maser sources tends to decrease with an increase of tge galactocentric distance.
4. The data in the present and previous SiO maser surveys give a local inclination of the rotation curve which is consistent with values obtained previously in observations of the other kind of disk population stars and a HI gas component.

The authors thank the staff of the Nobeyama radio observatory for their help during observations, and also thank Y. Ita and T. Soma for their help in the data reductions. The authors also thank an anonymous referee, who gave many useful comments and suggestions. This research has made use of the SIMBAD database operated by CDS and MSX database in IPAC. This paper is a part of the JN's thesis presented for the award of Ph. D. to the Graduate University for Advanced Studies.

Appendix 1. Individual Sources

A.1.1. IRAS 18413+1354 (V837 Her)

An SiO maser from this source is extremely strong (12 K in the $J = 1$–0, $v = 1$ transition). This source is included in the catalog of nearby dusty AGB stars within 1 kpc (Jura, Kleinmann 1989). This source is also very bright at 12 μm (225 Jy) with IRAS LRS (IRAS Low Resolution Spectrum) class of 29. OH and H_2O masers have been detected (Slootmaker et al. 1985; Comoretto et al. 1990); ^{12}CO (1–0) was detected (Margulis et al. 1990); CS (1–0) and NH_3 (1, 1) searches were negative (Anglada et al. 1996).

A.1.2. IRAS 18530+0817 (EIC 719)

An IRAS LRS of this source exhibits an unusual spectrum (LRS class 04; 04 means strange band shape). It has strong silicate emission peaking near 9 μm (Olnon, Raimond 1986), which is either self-absorption at 10 μm or the silicate feature affected by the other molecular bands. SiO masers were detected in the present work. An OH search was negative (Lewis et al. 1990). This object has the strongest stellar photospheric H_2O absorption, yet observed in the near-infrared (Walker et al. 1997).

A.1.3. IRAS 18581+1405

The observed radial velocity, $V_{\rm lsr} = 124.4$ km s^{-1}, of this source is somewhat high for a disk population star (highest in figures 7 and 8). The main-line of OH maser (1665 MHz) was detected at $V_{\rm lsr} = 114.4$ km s^{-1} (Lewis 1997), which is consistent with the SiO radial velocity. A H_2O maser search was negative (Engels, Lewis 1996).

A.1.4. IRAS 18585+0900

The IRAS LRS class of this source is 41 (indicating a carbon star). However, this is due to absorption at the 10 μm silicate feature. In fact, SiO maser emission (only the $J = 1$–0, $v = 2$ transition) was detected in the present work. Double peaks of the OH maser (1612 MHz) gave an expansion velocity of 61 km s^{-1} (Eder et al. 1988), whereas the expansion velocity in the CO observation was 20 km s^{-1} (Loup et al. 1993). The H_2O maser was negative (Engels, Lewis 1996).

A.1.5. IRAS 19192+0922 (AFGL 2374)

Based of the radio observations of ^{12}CO ($J = 1$–0 and $J = 2$–1 transitions; Heske et al. 1990), the mass-loss rate of this source was estimated to be 9.0×10^{-6} $M_{\odot}$ yr^{-1}. The distance to this source, 1.13 kpc, was obtained by an OH phase lag measurement (van Langevelde et al. 1990). The distance (1.6 kpc) used in the present work is consistent with this value. An IRAS LRS class is 31. Meixner et al. (1999) selected this source as a proto-planetary nebula candidate. Because we detected SiO masers in this star, this source might still be in the AGB phase.

A.1.6. IRAS 19229+1708

The profile of SiO masers of this source is somewhat unusual, exhibiting a relatively wide line width and multiple peaks in the $J = 1$–0, $v = 1$ line, which is stronger than that of $v = 2$. A H_2O maser has been detected (Engels, Lewis 1996).

A.1.7. IRAS 19371+2855 (NSV 12260)

This star was classified as an S-type star, based on the presence of the (0,0) subbands of the optical region of LaO (Stephenson 1990), but reclassified by Lloyd Evans, Little-Marenin (1999) as a late M-type star. SiO maser detection in the present work and a strong silicate emission (Lloyd Evans, Little-Marenin 1999) are consistent with the non-S-type. The thermal lines of CO (1–0 and 2–1) were also detected at $V_{\rm lsr} \simeq 20$ km s^{-1} (Groenewegen, de Jong 1998), which is consistent with $V_{\rm lsr} = 24.3$ km s^{-1} in the present work. OH and H_2O have been detected (Chengalur et al. 1993; Engels, Lewis 1996).

A.1.8. IRAS 19558+3333

This is a suspected symbiotic star. Radio continuum emission from this source implies a hot, ionizing companion (Seaquist, Ivison 1994). A search for the 3.1 μm absorption feature, a characteristics of carbon stars, was negative (Groenewegen et al. 1994). SiO (present work) and OH (Le Squeren et al. 1992) maser searches were negative.

A.1.9. IRAS 20056+1834 (QY Sge)

The optical counter part of this source is a G0 supergiant with a visual magnitude of 12.5, indicating a post-AGB star. The spectrum has very strong, broad Na D emission lines (Menzies, Whitelock 1988). An SiO maser search was negative in the present work.

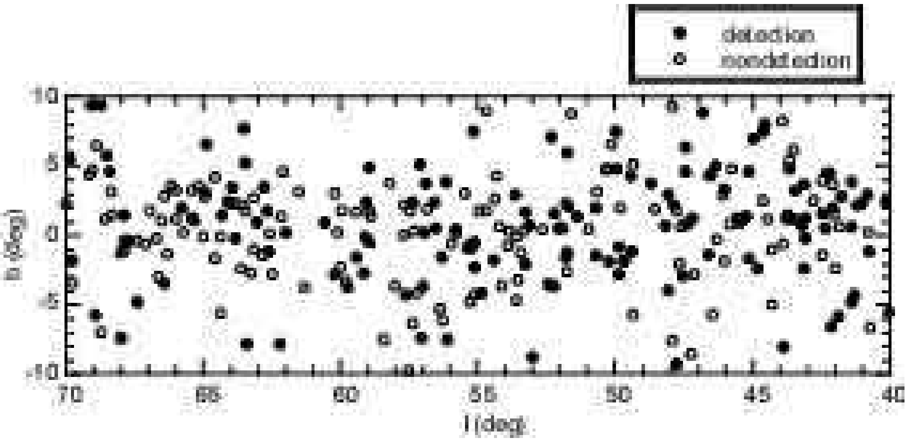

Fig. 1. Distribution of observed sources in the galactic coordinates. The filled and open circles indicate the SiO detection and non-detection, respectively.

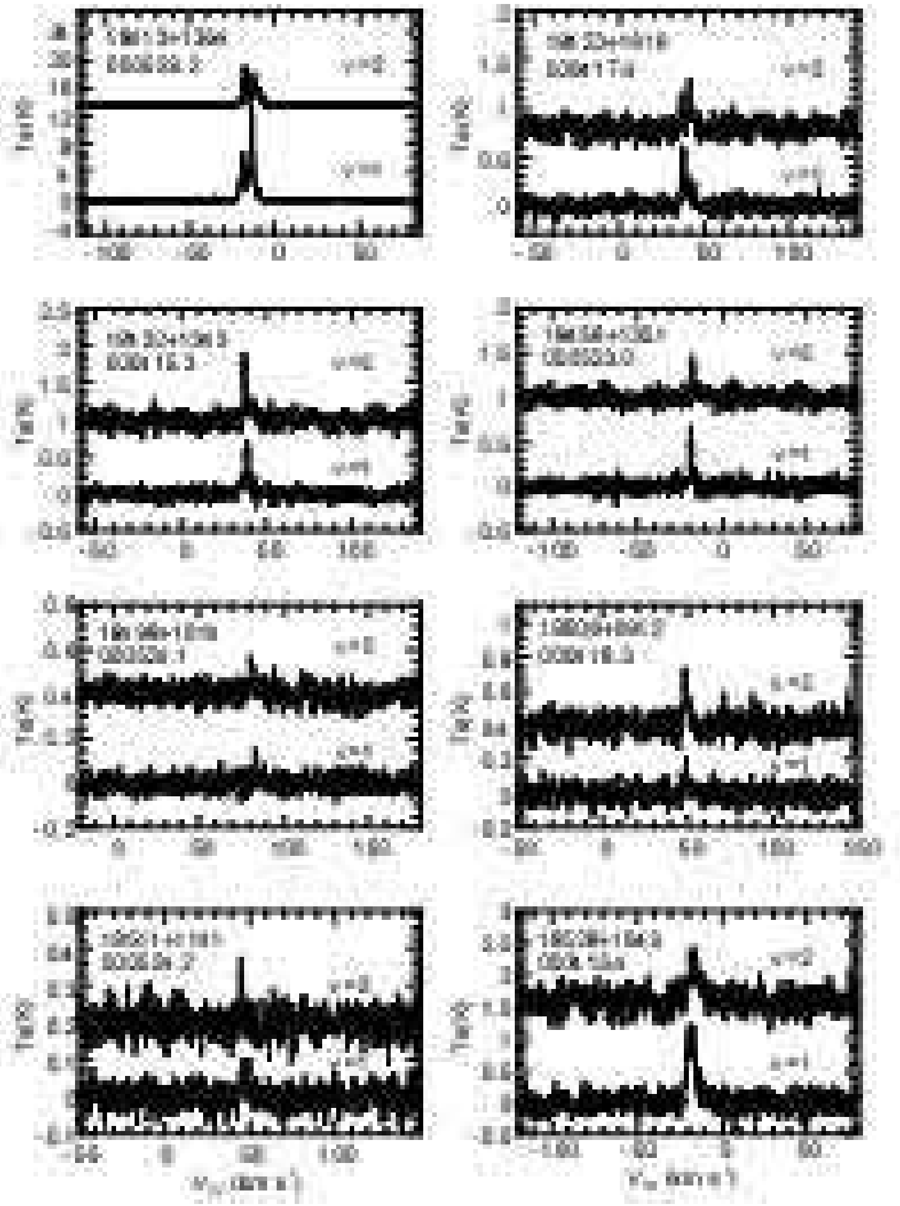

Fig. 2a. Spectra of the SiO $J = 1$–0, $v = 1$ and 2 lines for 134 detected sources.

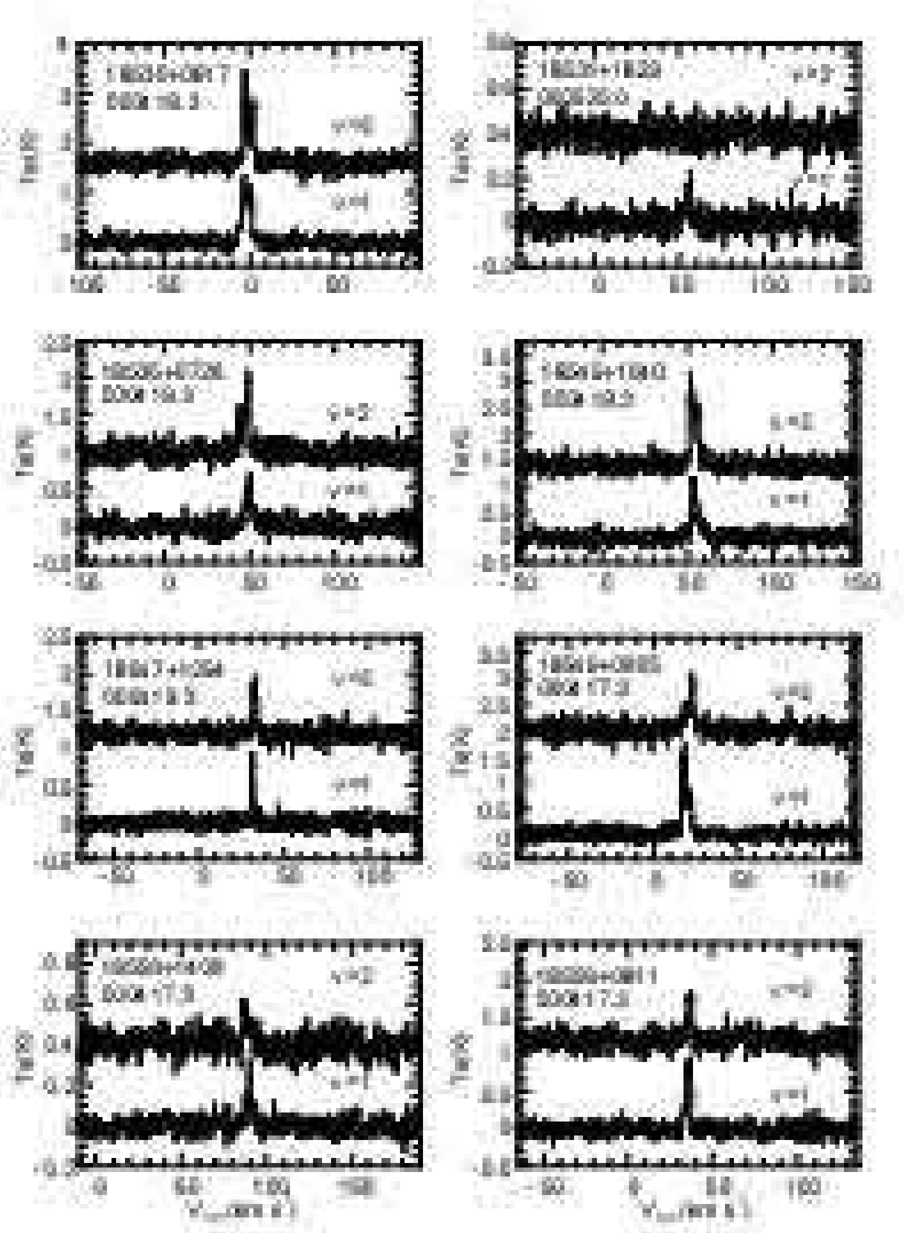

Fig. 2b. Continued.

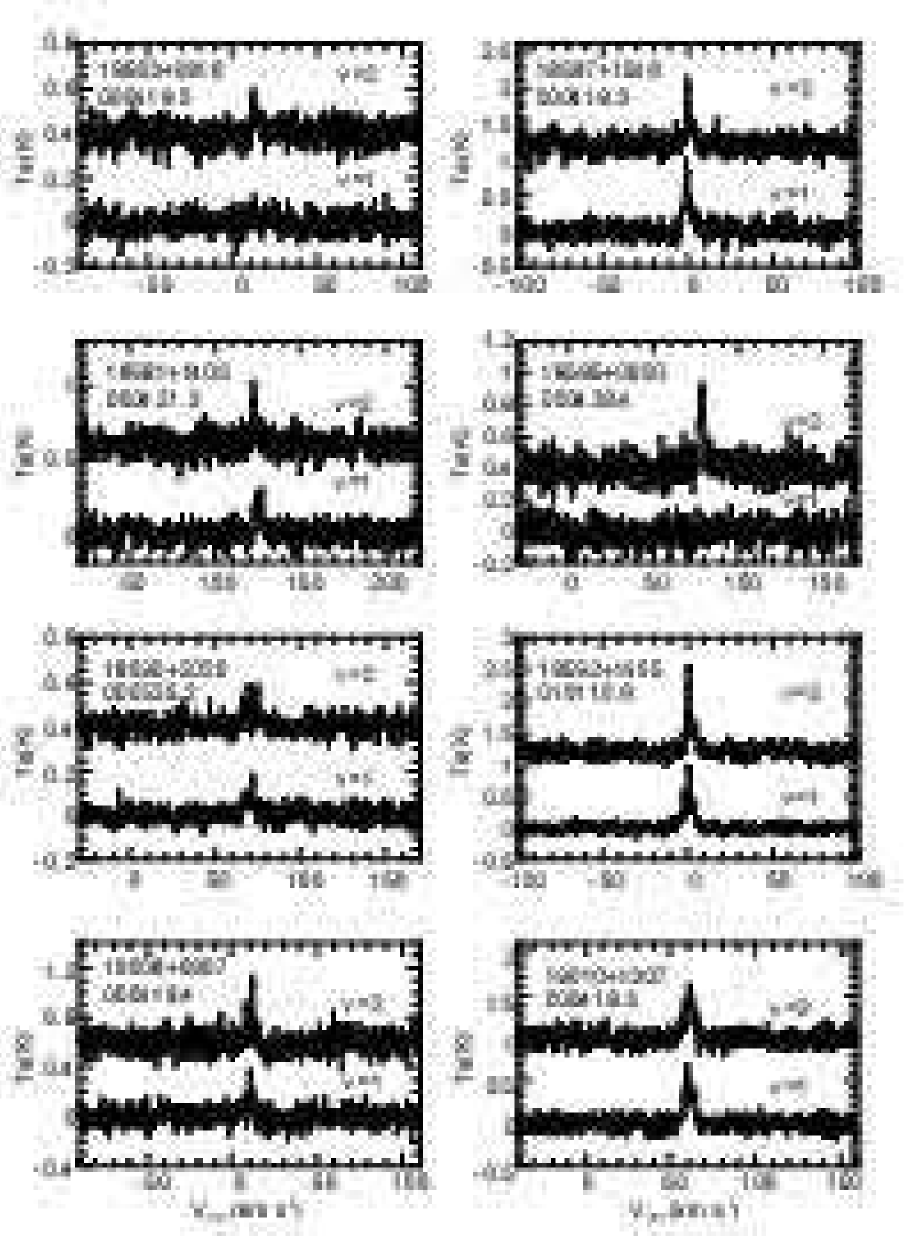

Fig. 2c. Continued.

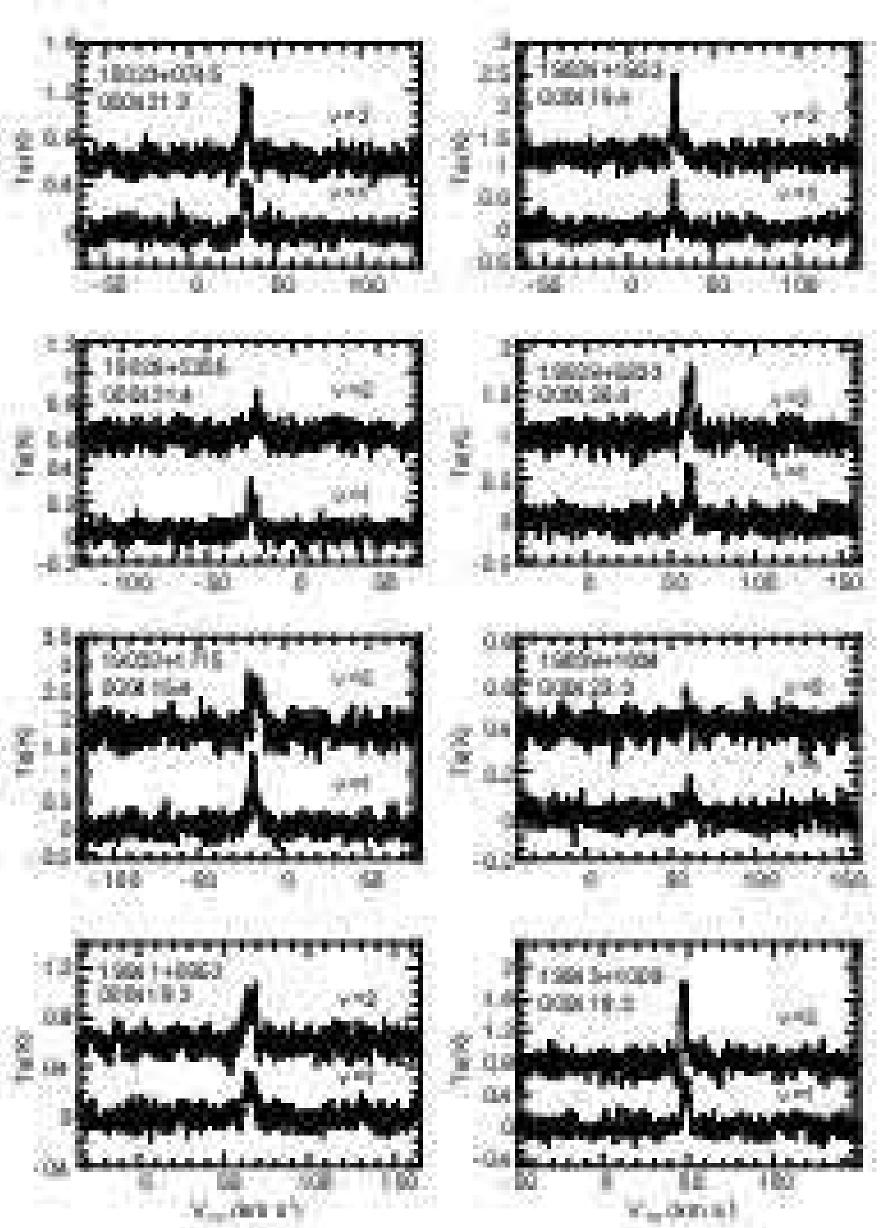

Fig. 2d. Continued.

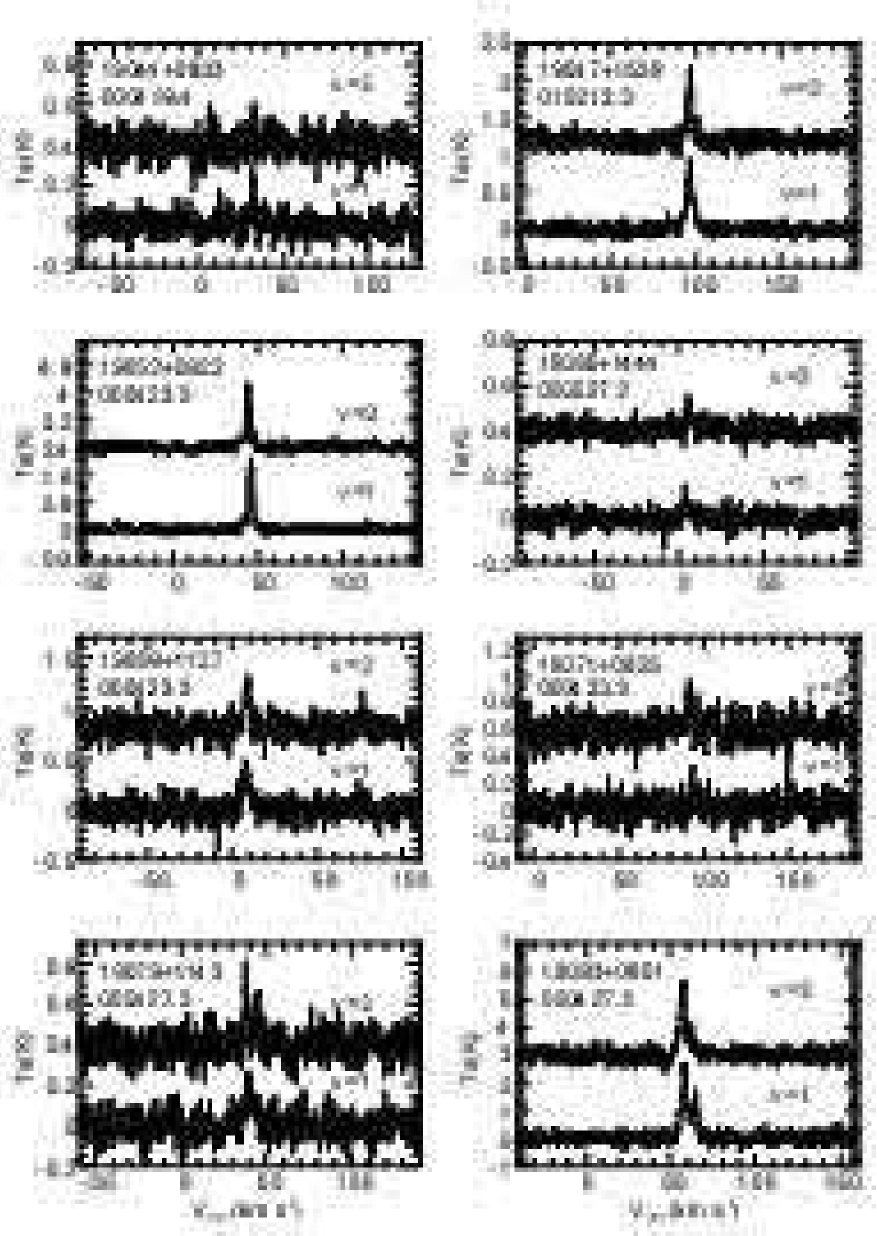

Fig. 2e. Continued.

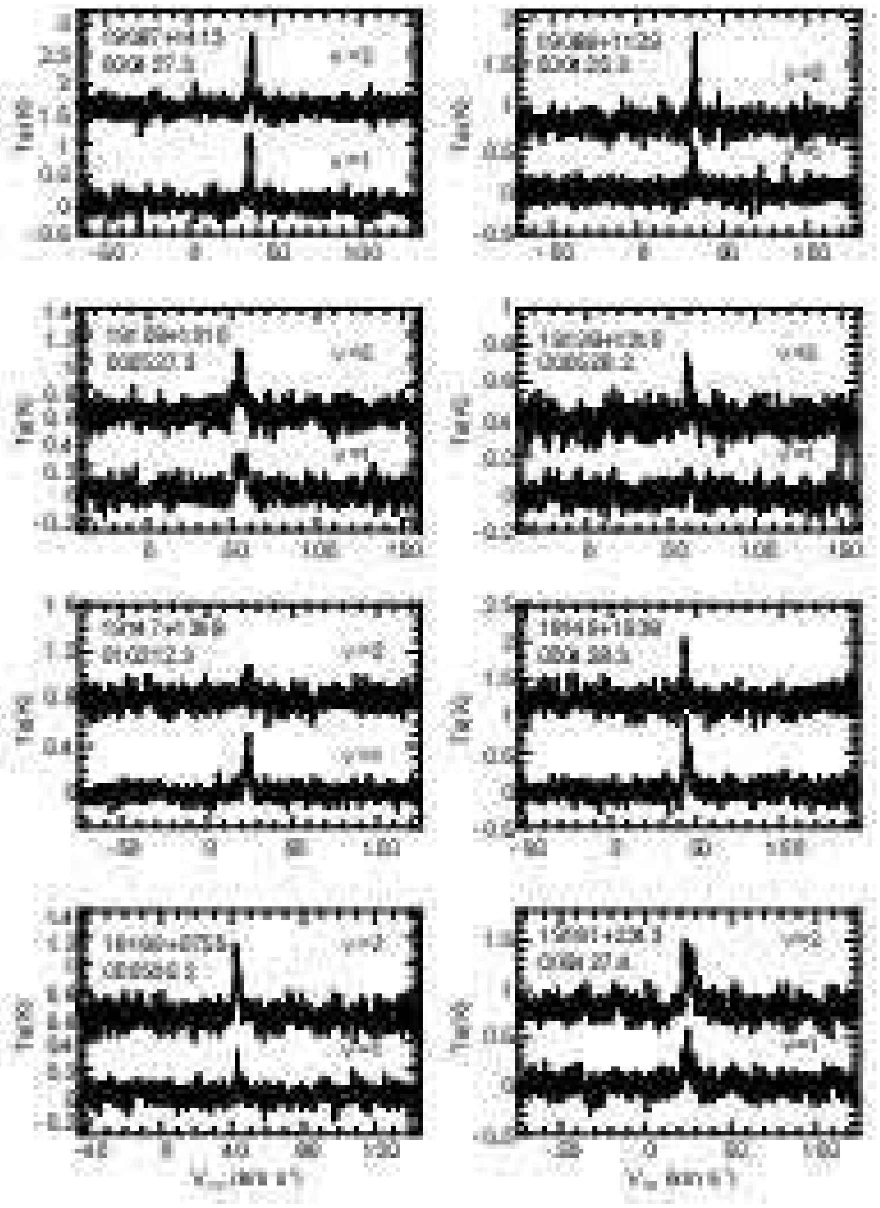

Fig. 2f. Continued.

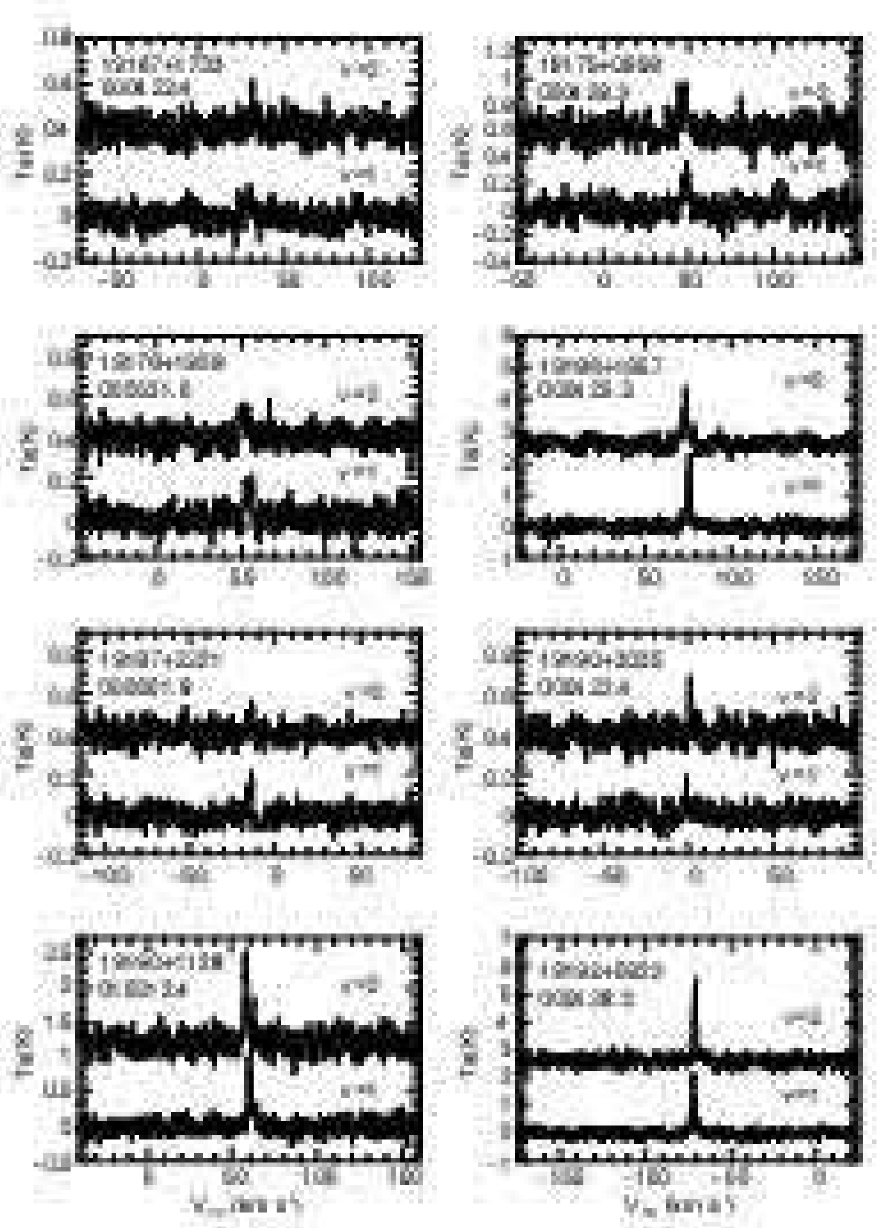

Fig. 2g. Continued.

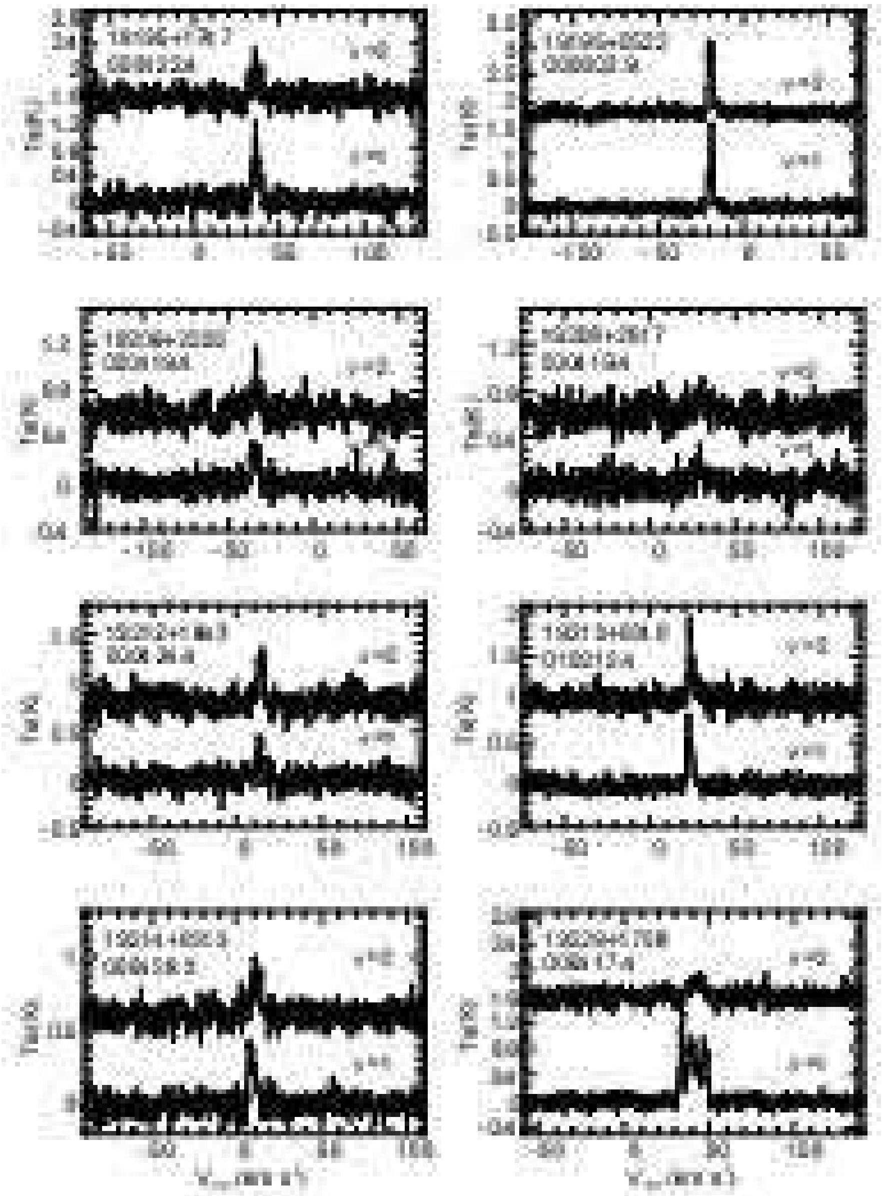

Fig. 2h. Continued.

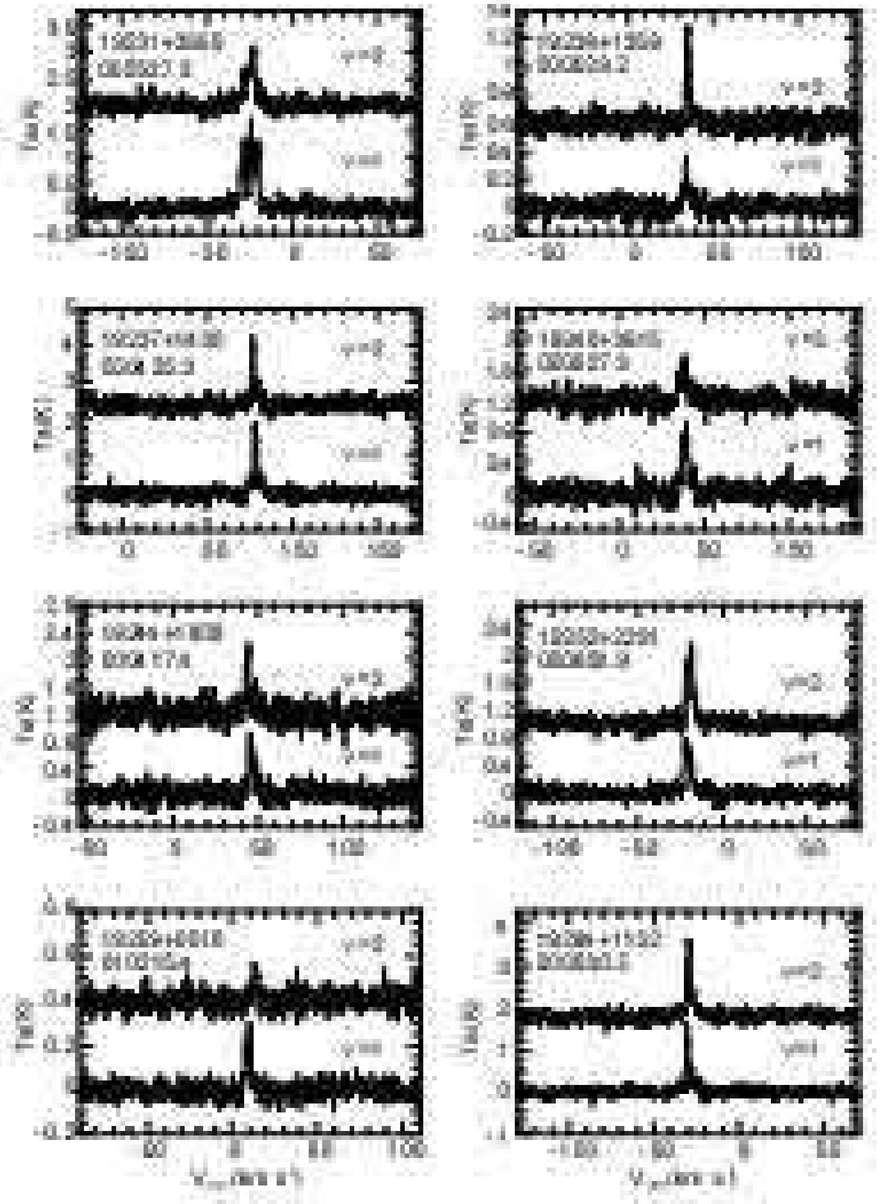

Fig. 2i. Continued.

figjb.eps

Fig. 2j. Continued.

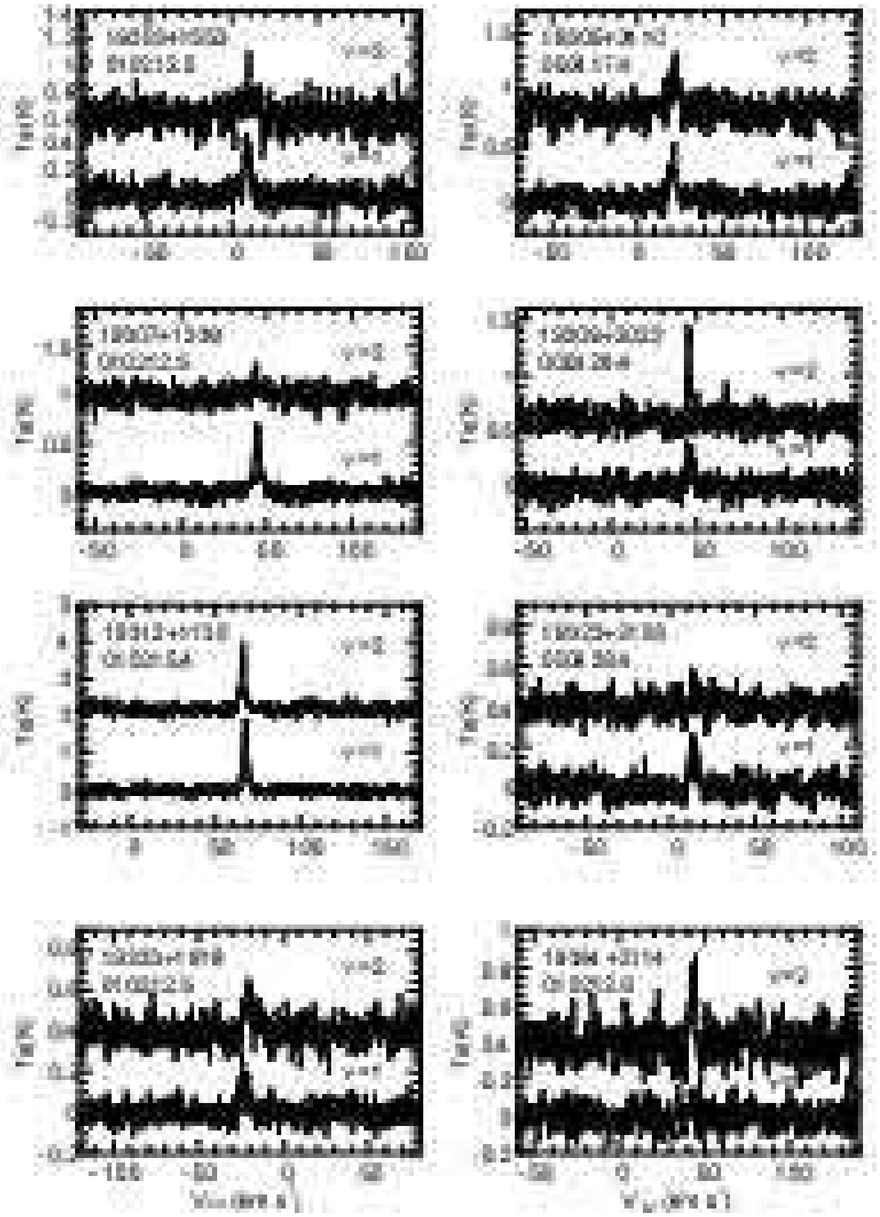

Fig. 2k. Continued.

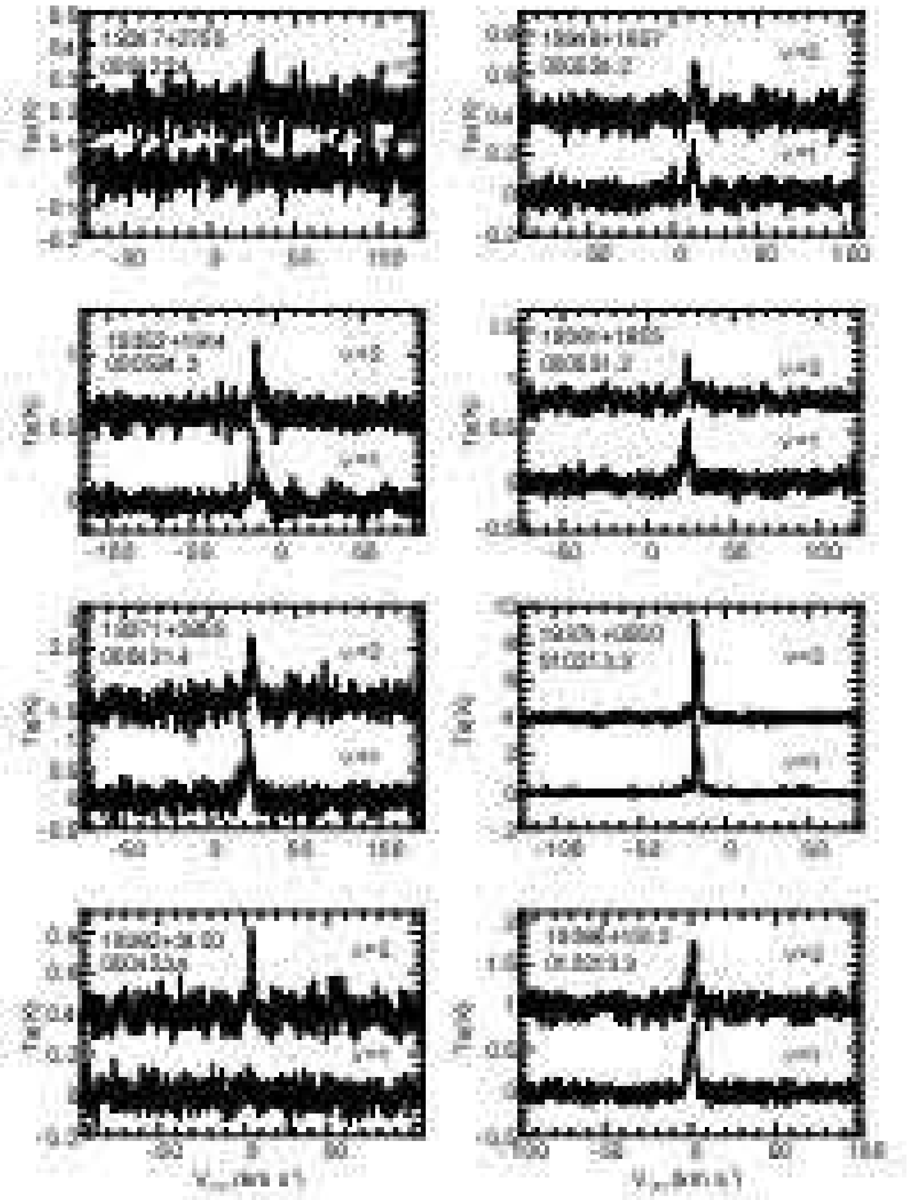

Fig. 2l. Continued.

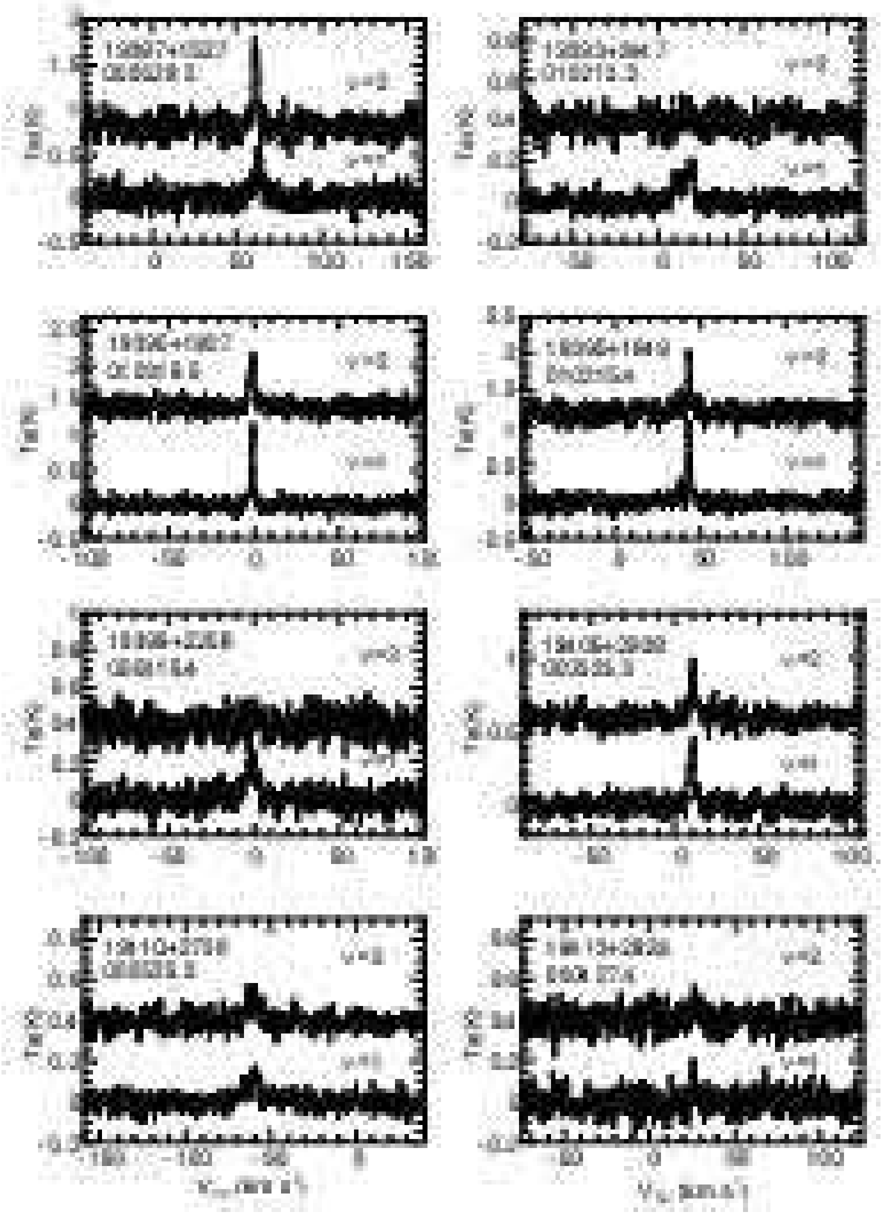

Fig. 2m. Continued.

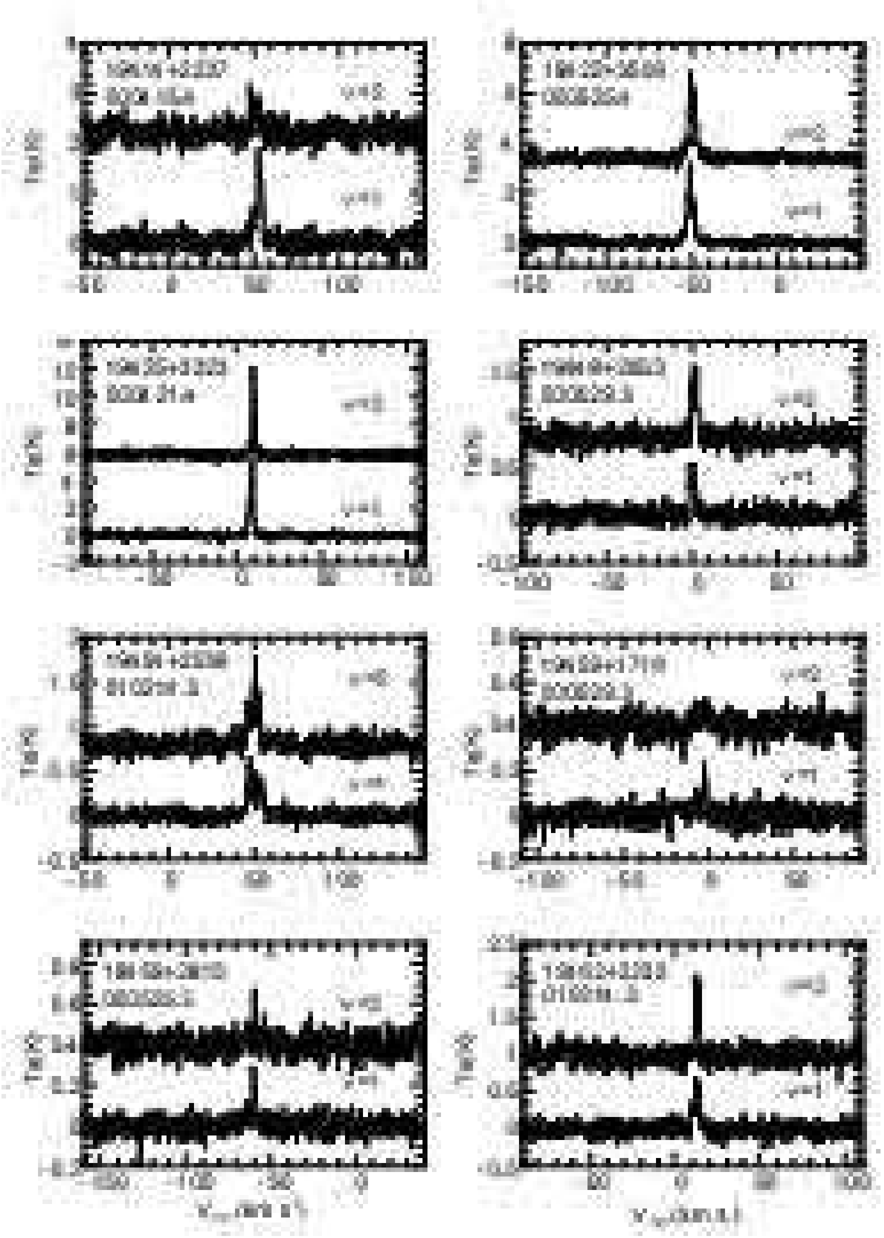

Fig. 2n. Continued.

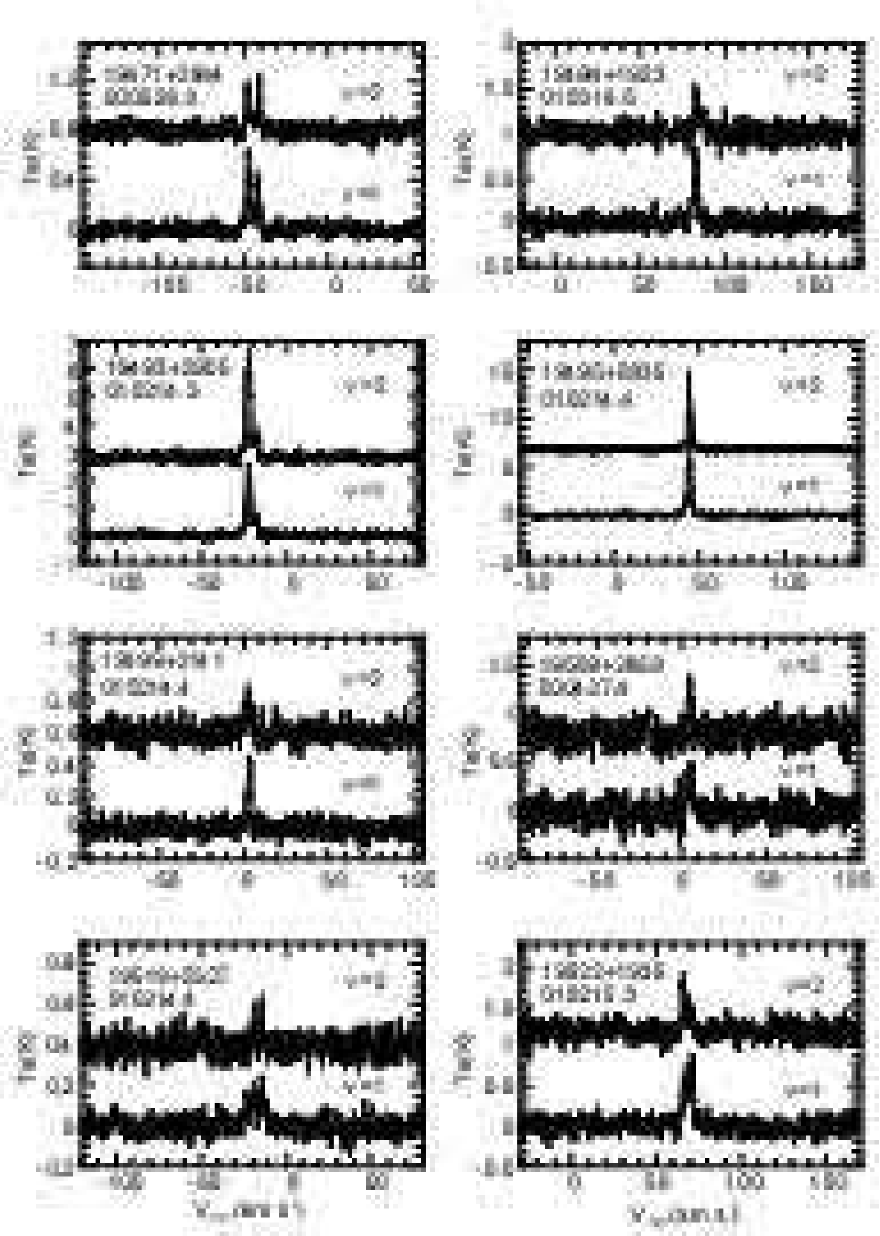

Fig. 2o. Continued.

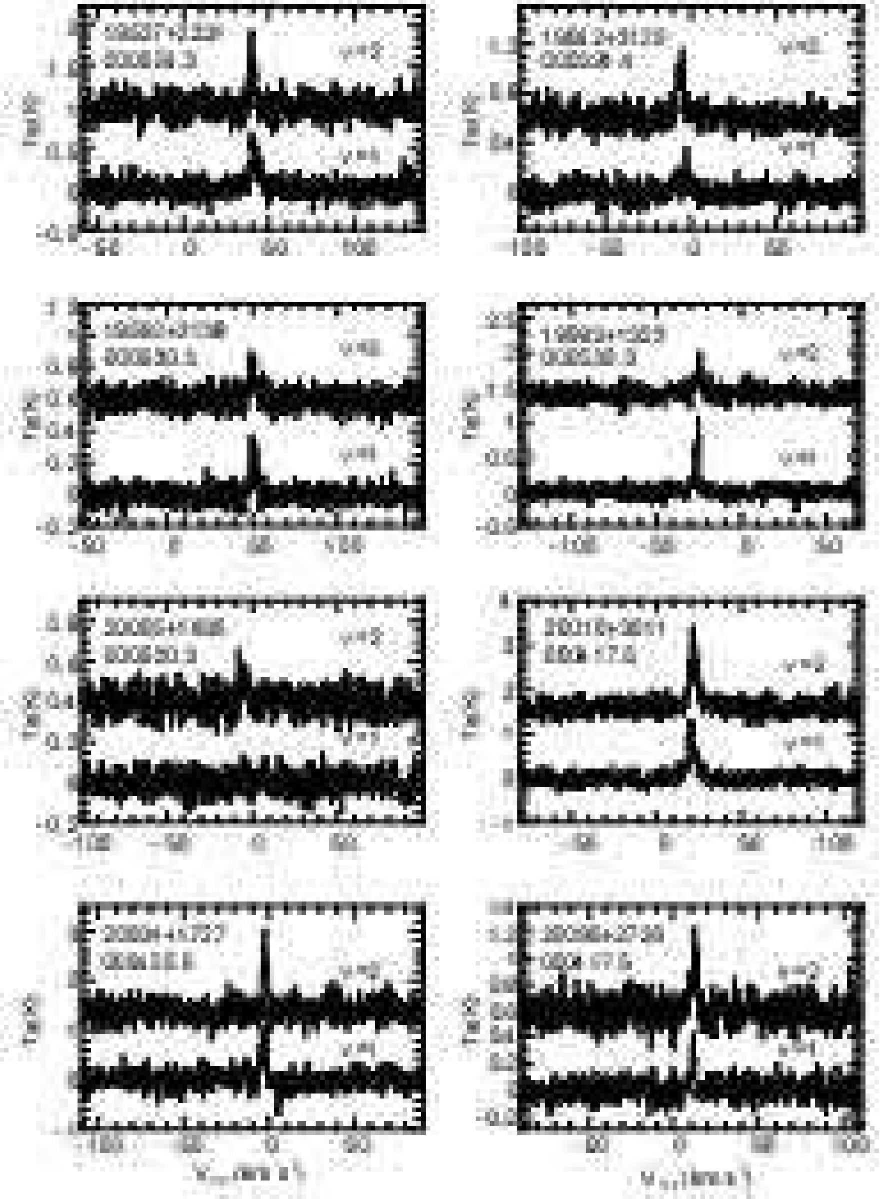

Fig. 2p. Continued.

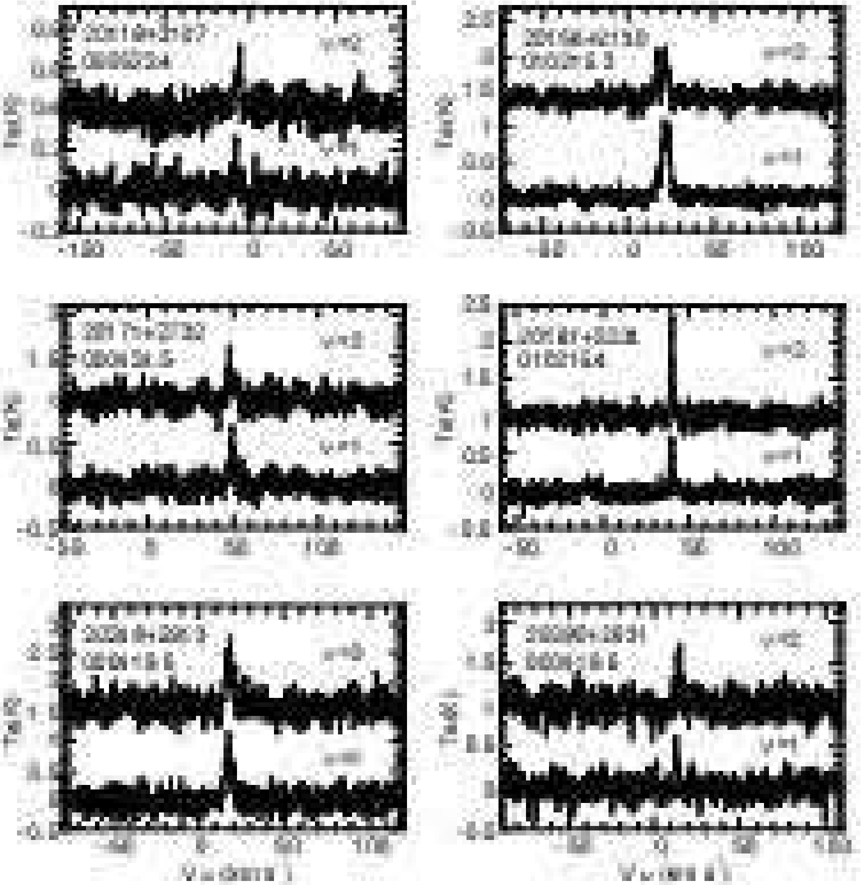

Fig. 2q. Continued.

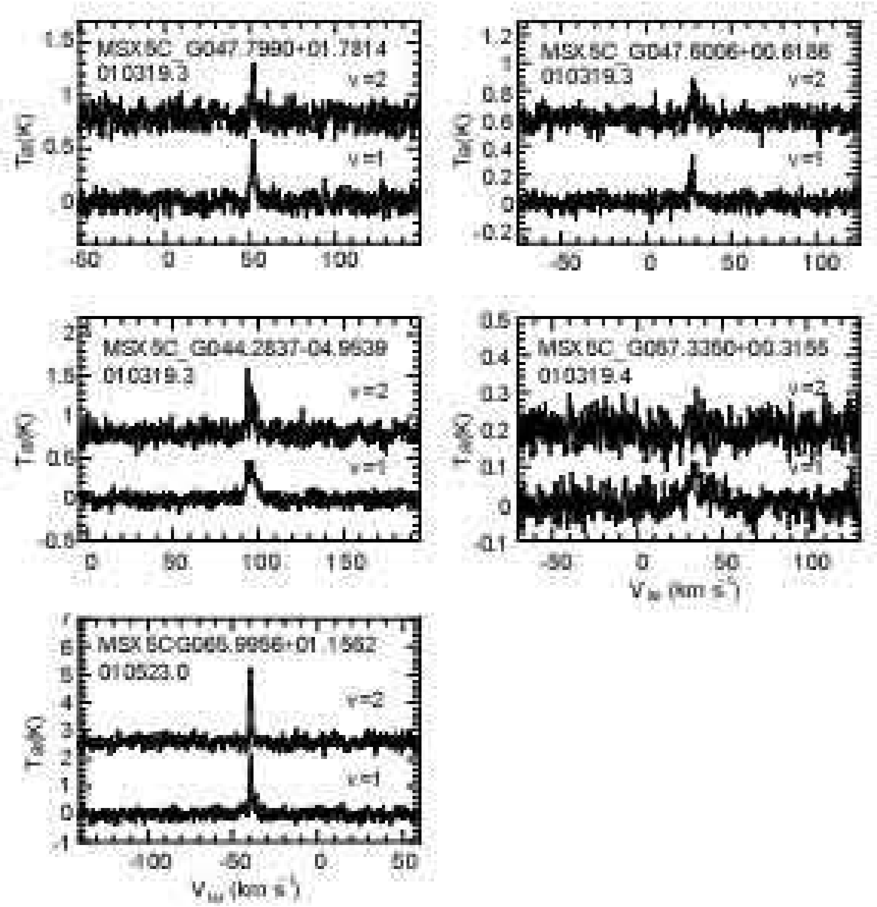

Fig. 3. Spectra of the SiO $J = 1$–0, $v = 1$ and 2 lines for MSX sources as counterparts of IRAS PSC with large position uncertainties.

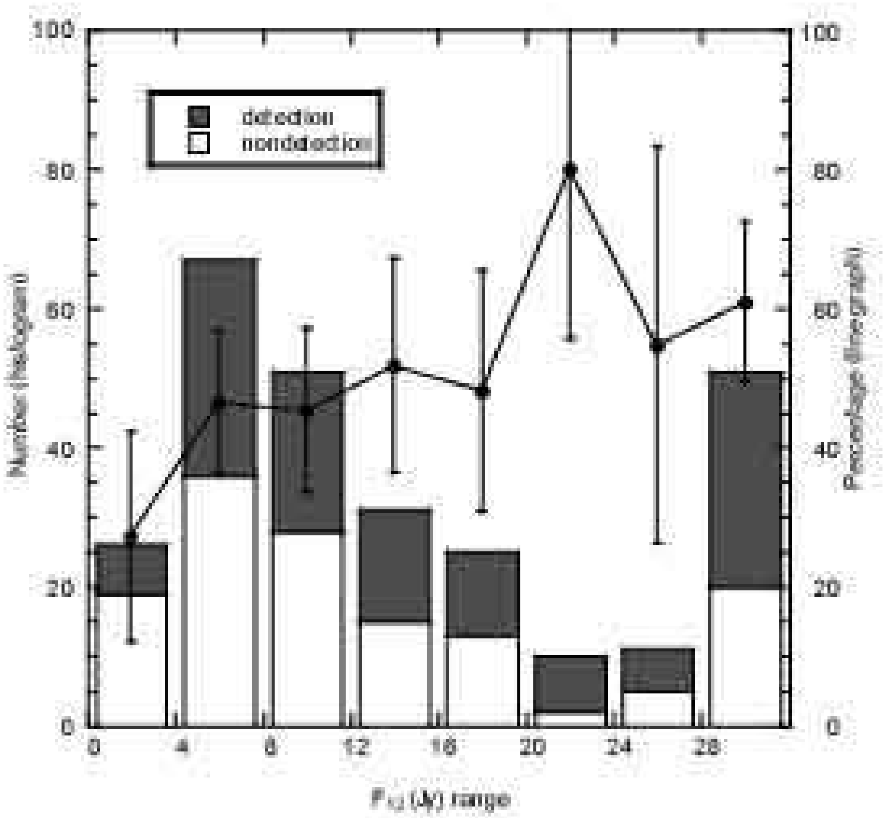

Fig. 4. Histogram of the 12 μm flux density (bar graph) and detection rate as a function of the IRAS 12 μm flux density (line graph). Error bars in the line graph mean 90% confidence intervals.

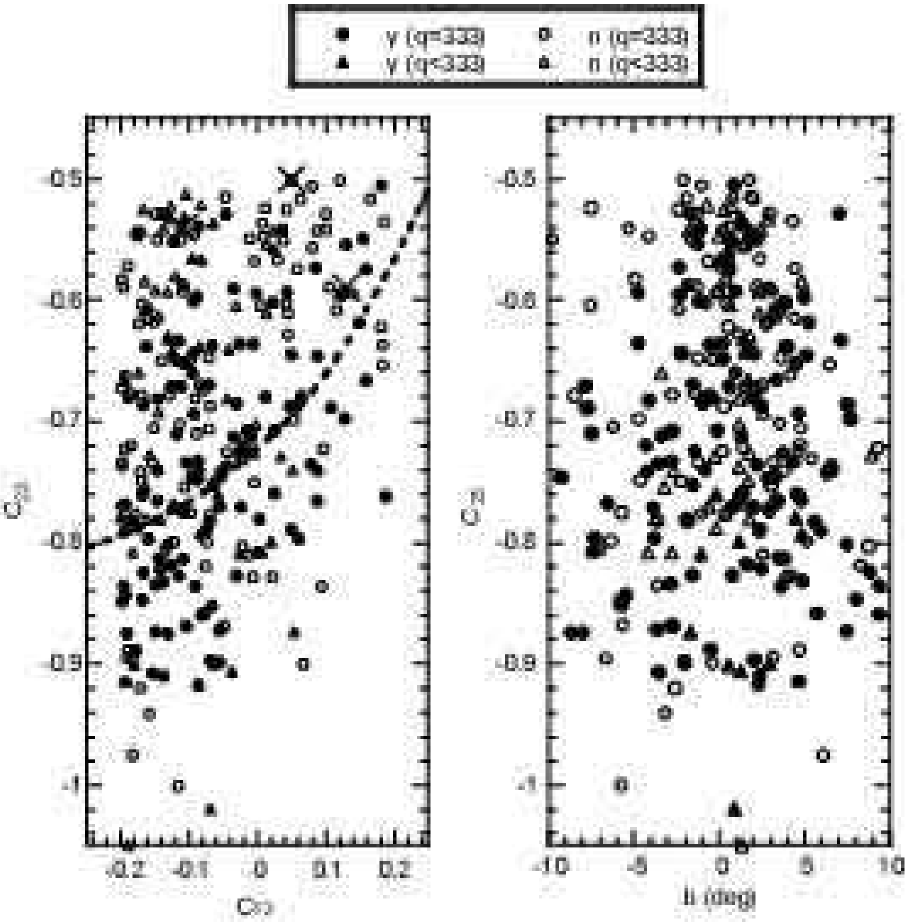

Fig. 5. Two color (C_{23}–C_{12}; left panel) and color-latitude (C_{23}–b; right panel) diagram for the observed sources. The dotted line indicates an evolutionary track of the O-rich AGB star (van der Veen, Habing 1988).

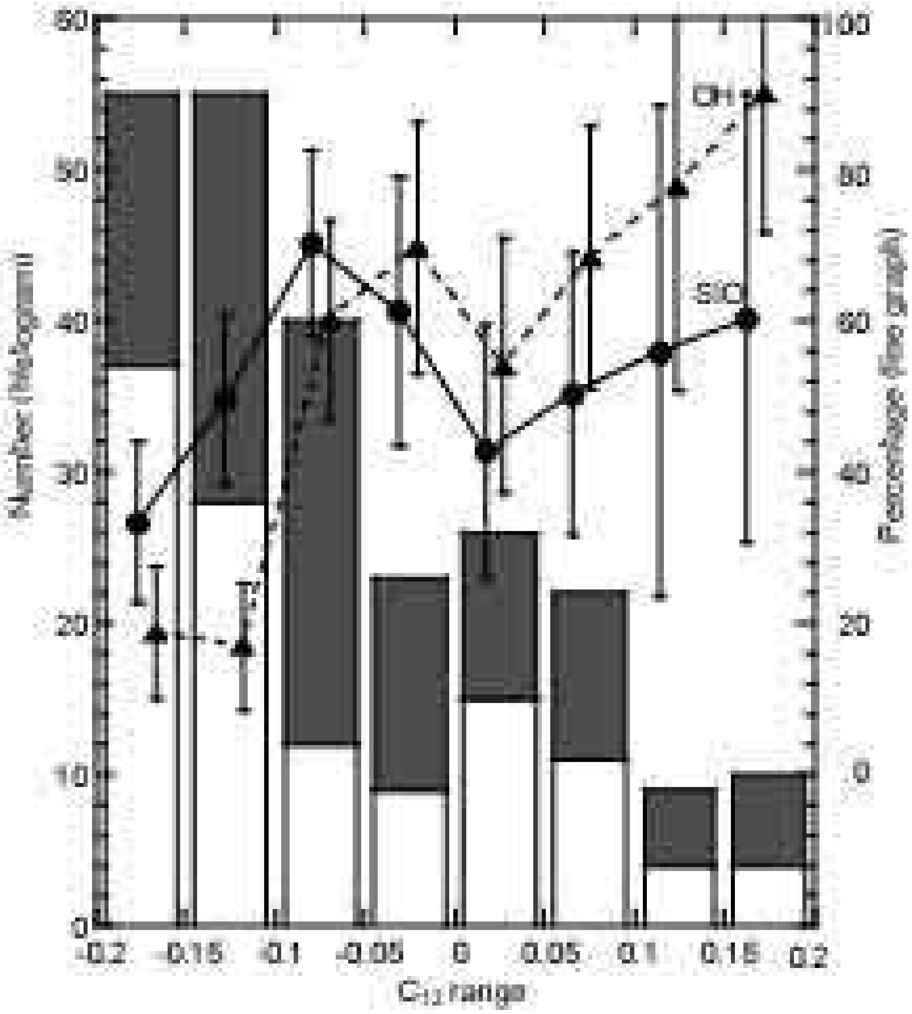

Fig. 6. Histogram of the color index, C_{12} (bar graph), and detection rate as a function of the C_{12} for SiO maser search (solid line) and OH maser searches (dotted line). Shaded portions in columns indicate the number of detections of SiO and OH masers. Error bars in line graphs mean 90% confidence intervals.

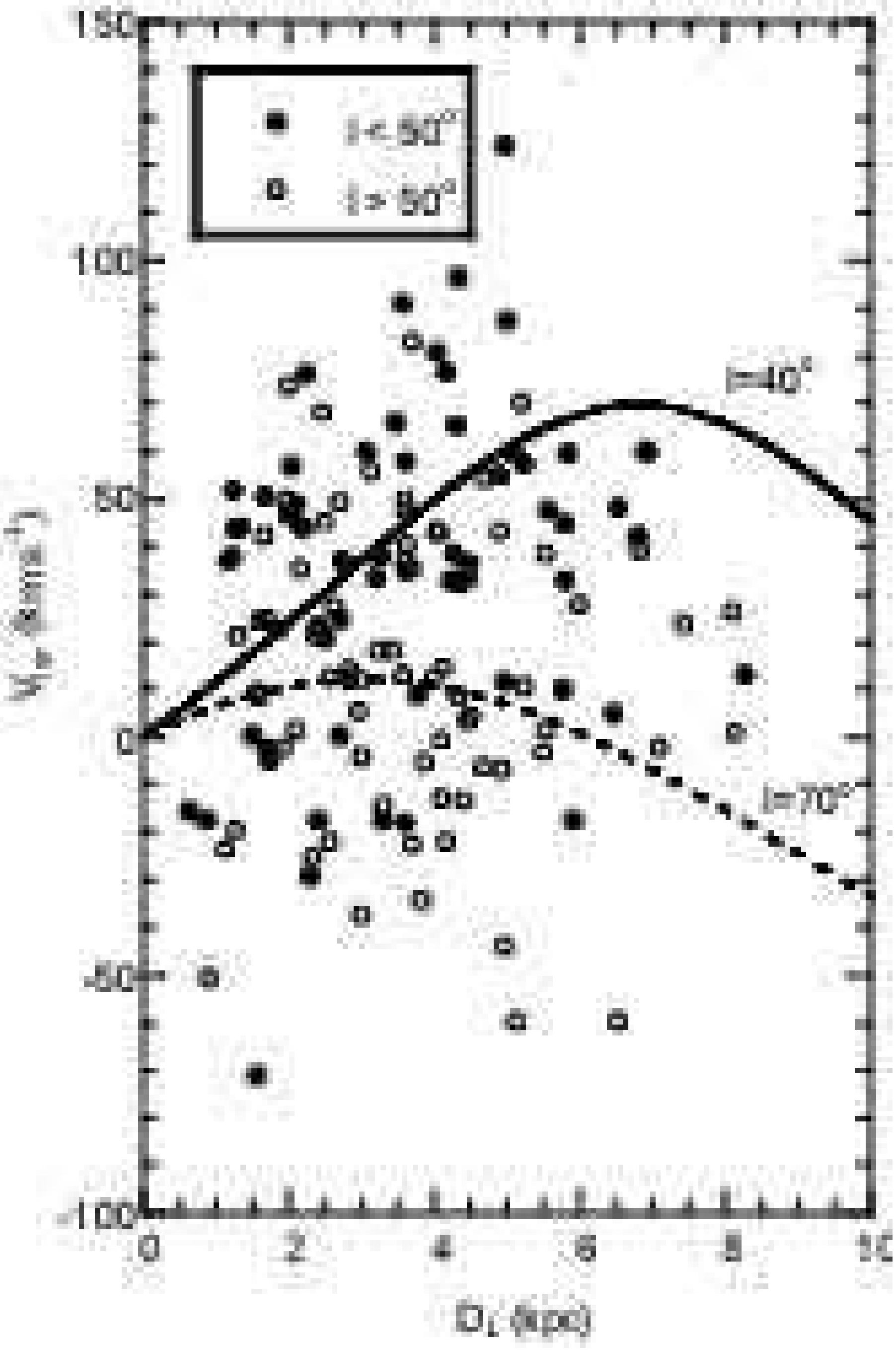

Fig. 7. Observed radial velocity versus the luminosity distance. The solid and dotted curves are the radial velocities expected at $l = 40°$ and $70°$, respectively, from the Galactic rotation curve $V_{\rm rot} = 220{\rm km\,s}^{-1} R(8.5 + R_{\rm a})/[8.5(R + R_{\rm a})]\{1 + 1.1/[1 + 3(R - R_{\rm a})^2]\}$, where R is the distance from the Galactic center in kpc and $R_{\rm a}$ is an adjustable parameter (assumed to be 0.3 kpc) that creates a peak of the rotation curve near $R_{\rm a}$.

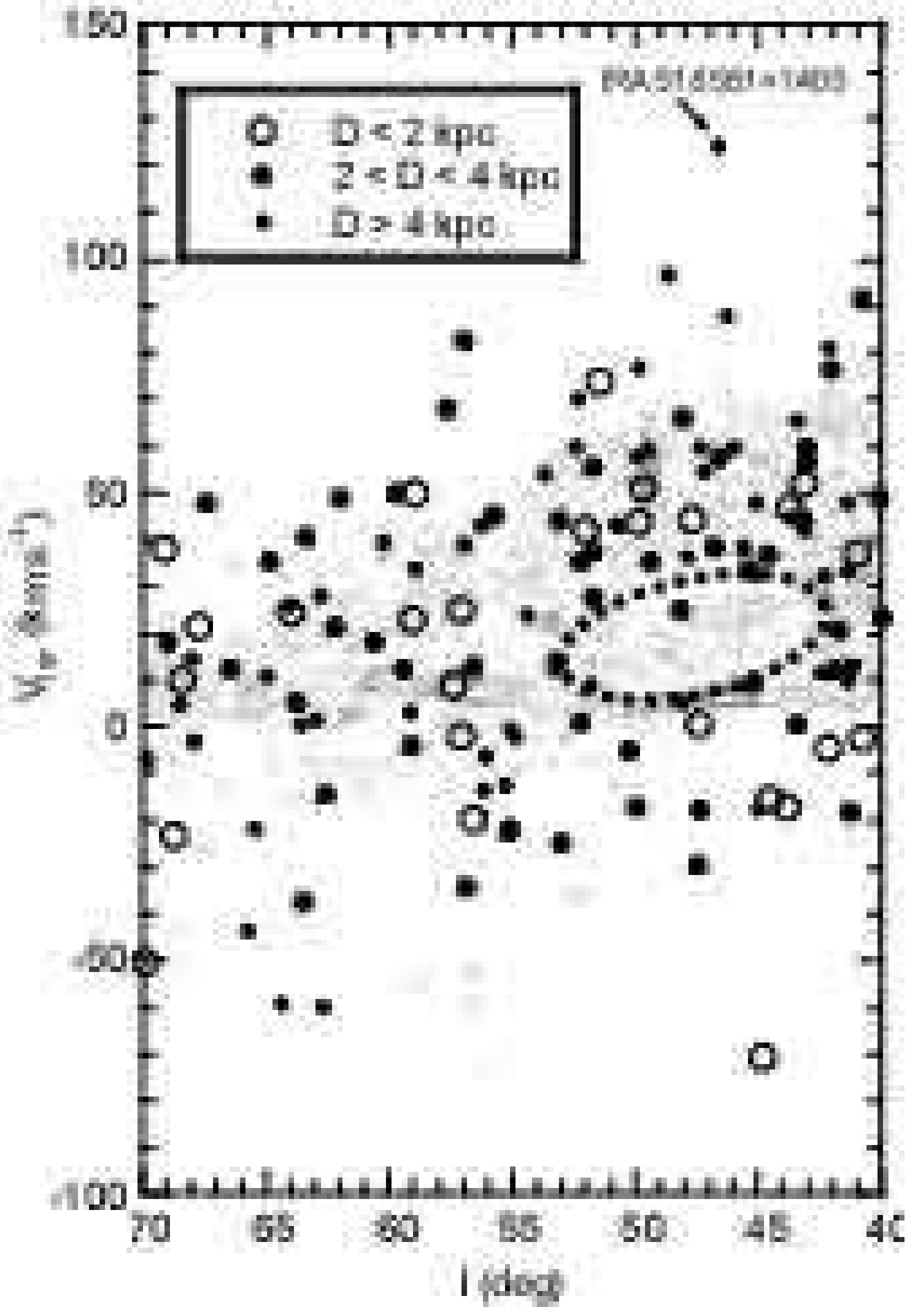

Fig. 8. Longitude–velocity diagram of the SiO detected sources overlaid on the CO v–l map, integrated in the range between $b = \pm 3^{\circ}\!.25$ (taken from Dame et al. 1987). The region surrounded by the dotted ellipse indicates a source vacant area (see text).

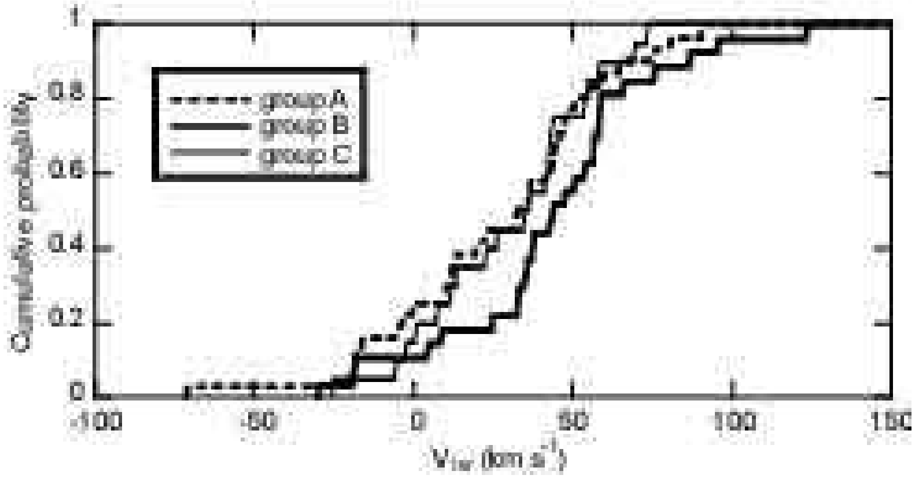

Fig. 9. Cumulative probability plot of the V_{lsr} distribution of the present sample. The cumulative probability is shown for three groups (see text).

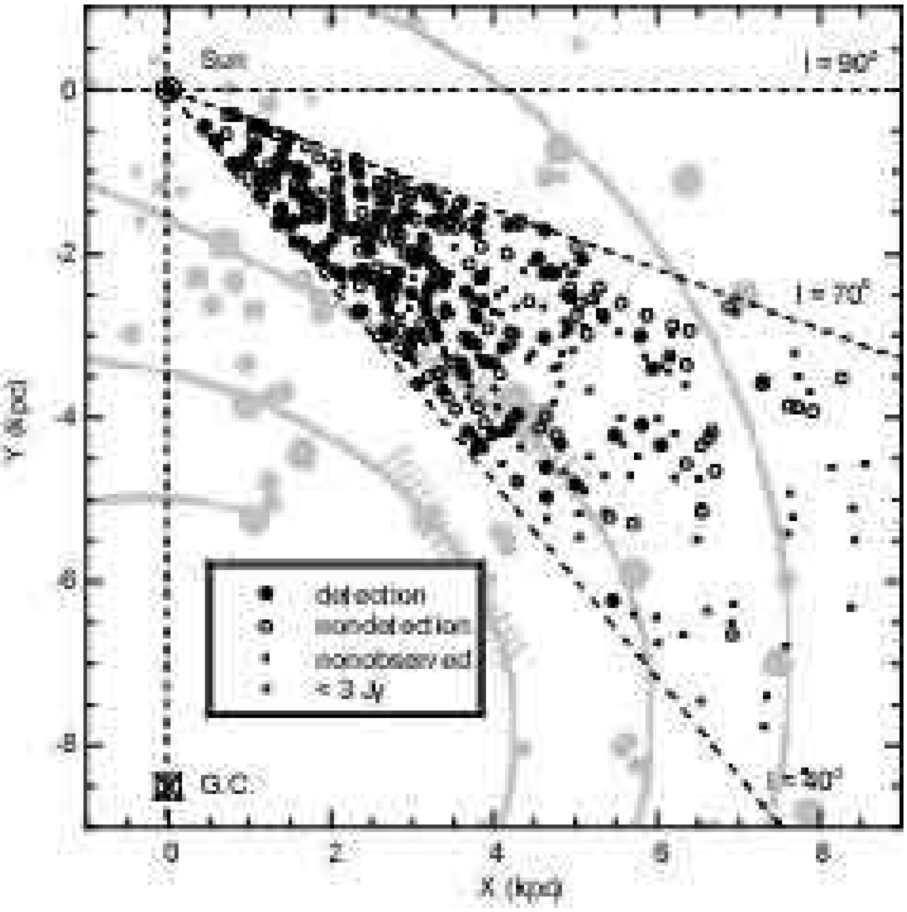

Fig. 10. Positions of the observed sources projected onto the galactic plane, overlaid on the spiral model of the Galaxy (Taylor, Cordes 1993). The positions of the Sun and the Galactic center are at the origin and $(X, Y) = (0, -8.5)$, respectively.

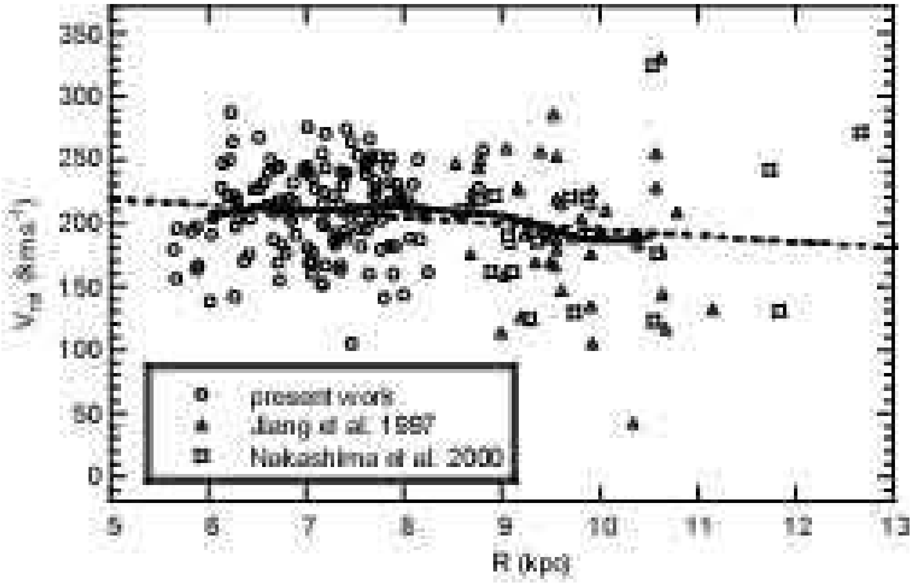

Fig. 11. Rotation curve of SiO maser sources. The solid line indicates the running mean of the data.

Table 1. List of detections.

		$J = 1$–0	$v = 1$			$J = 1$–0	$v = 2$		
IRAS name	$V_{\rm lsr}$	$T_{\rm a}$	S	r.m.s.	$V_{\rm lsr}$	$T_{\rm a}$	S	r.m.s.	Obs. date
	(km s^{-1})	(K)	(K km s^{-1})	(K)	(km s^{-1})	(K)	(K km s^{-1})	(K)	(yymmdd.d)
18413+1354	−12.9	13.364	47.770	0.084	−17.9	5.335	31.542	0.099	000529.2
18423+1616	35.9	0.595	2.216	0.052	40.8	0.495	1.368	0.071	000417.4
18432+1343	37.1	0.712	2.323	0.058	37.2	0.878	2.116	0.080	000415.3
18456+1351	−17.3	0.730	1.428	0.054	−17.7	0.516	0.895	0.064	000523.0
18498+1014	81.5	0.149	0.395	0.029	80.8	0.185	0.524	0.034	000524.1
18506+0912	47.8	0.225	0.250	0.043	48.1	0.334	0.541	0.052	000418.3
18511+1141	45.0	0.101	0.361	0.027	44.8	0.180	0.028	0.033	000524.2
18528+1543	−18.3	1.293	6.896	0.122	−16.6	0.835	4.528	0.157	000415.4
18530+0817	−2.1	1.382	6.700	0.095	−2.6	1.851	7.040	0.105	000418.3
18531+1829	55.2	0.229	0.670	0.039	···	···	···	0.044	000525.0
18535+0726	49.0	0.757	2.839	0.081	48.9	1.080	3.930	0.100	000419.3
18545+1040	52.1	1.155	5.043	0.090	51.7	1.775	7.484	0.105	000418.3
18547+1254	32.7	0.943	1.902	0.066	33.2	0.760	1.982	0.087	000419.3
18549+0905	19.4	1.701	7.022	0.081	22.3	1.087	4.366	0.126	000417.3
18556+0811	37.4	0.970	2.808	0.067	36.7	0.688	2.145	0.098	000417.3
18556+1409	88.4	0.328	0.835	0.032	87.1	0.217	0.924	0.050	000417.3
18563+0816	13.8	0.121	0.296	0.040	12.7	0.199	0.554	0.048	000419.3
18567+1046	0.5	0.995	3.493	0.088	0.1	0.917	2.394	0.106	000418.3
18581+1405	125.9	0.297	0.934	0.053	122.5	0.431	1.082	0.067	000421.3
18585+0900	···	···	···	0.061	78.4	0.526	2.066	0.067	000426.4
18590+2025	70.4	0.183	0.822	0.027	69.8	0.188	0.866	0.033	000525.2
18592+1455	0.5	1.003	3.771	0.051	0.3	1.373	4.315	0.086	010110.6
19008+0907	11.4	0.414	1.083	0.062	11.5	0.534	1.033	0.074	000419.4
19010+1307	58.6	0.675	2.919	0.065	61.1	0.616	2.735	0.076	000418.3
19023+0745	31.3	0.441	1.814	0.058	34.8	0.740	2.740	0.072	000421.3
19024+1923	27.7	0.816	2.073	0.105	27.0	1.384	4.090	0.118	000419.4
19029+2305	−23.4	0.363	1.152	0.042	−21.3	0.282	0.888	0.053	000421.4
19029+0933	58.6	0.664	2.271	0.095	61.3	0.794	3.732	0.104	000426.4
19032+1715	−17.9	1.363	5.624	0.139	−16.9	1.003	2.911	0.182	000415.4
19039+1634	59.1	0.170	0.489	0.036	59.7	0.198	0.366	0.044	000422.3
19041+0952	62.4	0.396	1.798	0.061	68.4	0.463	2.399	0.070	000419.3
19043+1009	46.9	0.636	2.510	0.077	46.4	1.072	4.237	0.095	000418.3
19044+0833	32.4	0.287	0.797	0.047	32.4	0.205	0.336	0.058	000418.4
19047+1539	96.5	1.012	4.072	0.049	96.7	1.026	3.070	0.071	010212.3
19052+0922	44.7	2.077	6.356	0.066	43.7	1.803	5.908	0.077	000423.3
19065+1444	5.1	0.156	0.438	0.029	5.3	0.144	0.521	0.032	000527.2
19068+1127	9.3	0.491	2.123	0.089	9.1	0.570	1.883	0.093	000423.3
19071+0625	91.4	0.311	0.507	0.078	91.0	0.391	0.924	0.090	000423.3
19079+1143	39.6	0.284	1.252	0.057	37.6	0.403	1.356	0.063	000427.3

Table 1. (Continued)

		$J = 1$–0	$v = 1$			$J = 1$–0	$v = 2$		
IRAS name	$V_{\rm lsr}$	$T_{\rm a}$	S	r.m.s.	$V_{\rm lsr}$	$T_{\rm a}$	S	r.m.s.	Obs. date
	(km s^{-1})	(K)	(K km s^{-1})	(K)	(km s^{-1})	(K)	(K km s^{-1})	(K)	(yymmdd.d)
19083+0851	56.7	2.647	16.574	0.148	56.8	2.772	12.360	0.169	000427.3
19087+1413	36.4	1.225	3.591	0.108	36.4	1.192	2.513	0.113	000427.3
19088+1129	33.6	0.512	0.930	0.084	33.8	1.052	1.736	0.106	000425.3
19108+1310	55.6	0.307	1.757	0.057	53.9	0.481	1.954	0.064	000527.3
19128+1310	59.7	0.133	0.306	0.048	59.6	0.417	1.089	0.060	000529.2
19147+1349	25.1	0.509	1.573	0.049	24.9	0.285	1.049	0.072	010212.3
19149+1638	42.9	0.981	2.585	0.093	43.0	0.875	1.654	0.116	000428.3
19160+0755	42.2	0.320	0.581	0.055	42.2	0.539	1.626	0.068	000530.2
19161+2343	26.3	0.576	2.018	0.084	23.1	0.696	3.366	0.092	000427.4
19167+1733	42.9	0.103	0.297	0.038	31.6	0.222	0.367	0.046	000422.4
19175+0958	47.9	0.360	1.163	0.063	48.2	0.363	1.434	0.074	000428.3
19176+1939	54.6	0.204	0.361	0.049	53.8	0.185	0.513	0.044	000531.0
19186+1657	74.1	2.274	5.648	0.126	73.8	1.718	4.985	0.144	000425.3
19187+2221	−13.1	0.203	0.042	0.037	−14.0	0.177	0.386	0.041	000601.9
19190+3035	0.7	0.190	0.355	0.039	0.8	0.276	0.400	0.045	000422.4
19190+1128	58.2	1.003	2.708	0.083	57.6	1.315	3.478	0.128	010212.4
19192+0922	−70.9	2.232	5.462	0.120	−70.9	2.947	5.636	0.147	000428.3
19195+1747	35.1	1.227	3.685	0.107	35.5	0.755	2.557	0.118	000422.4
19195+0522	−17.6	1.614	4.095	0.067	−18.7	1.338	4.484	0.070	000602.9
19206+2255	−34.3	0.360	1.664	0.068	−33.9	0.560	1.308	0.082	000419.4
19206+2517	30.1	0.341	1.174	0.080	37.1	0.362	1.373	0.095	000419.4
19212+1843	14.0	0.470	1.263	0.076	13.9	0.601	1.404	0.093	000424.4
19213+0340	23.4	0.828	2.320	0.064	23.3	0.965	2.580	0.088	010212.4
19214+0513	9.7	0.430	1.713	0.052	10.3	0.390	1.953	0.063	000428.3
19229+1708	38.8	0.989	8.360	0.065	45.1	0.360	2.255	0.090	000417.4
19231+3555	−23.5	1.694	10.855	0.087	−23.3	1.112	6.367	0.096	000527.3
19236+1359	35.3	0.386	1.054	0.043	35.0	0.688	1.816	0.051	000529.2
19237+1430	76.8	1.991	4.812	0.117	76.8	1.834	4.449	0.132	000425.3
19240+3615	38.7	0.900	3.379	0.086	37.3	0.574	2.380	0.094	000527.3
19244+1809	44.4	0.888	2.888	0.096	44.4	1.107	3.280	0.132	000417.4
19252+2201	−21.0	0.783	3.479	0.067	−18.2	1.121	4.828	0.065	000604.9
19259+0510	11.2	0.311	0.801	0.030	13.0	0.163	0.186	0.038	010215.4
19264+1132	−29.2	1.625	4.514	0.074	−29.5	1.892	5.362	0.098	000530.2
19265+3116	34.3	0.377	1.649	0.055	36.8	0.445	0.635	0.069	000422.4
19270+2239	7.5	0.827	3.137	0.099	10.1	0.791	4.393	0.125	000417.4
19271+1354	51.0	3.350	8.386	0.106	50.9	2.832	7.158	0.107	000531.1
19276+1500	42.9	0.817	2.808	0.056	43.2	1.445	4.067	0.066	000604.9
19283+1421	−5.1	0.752	2.104	0.083	−4.8	1.451	3.453	0.106	000529.2
19288+2923	−37.7	0.810	2.253	0.088	−37.4	1.382	3.369	0.111	000420.4
19290+1600	55.8	0.262	1.260	0.050	55.8	1.177	1.997	0.067	010215.4

Table 1. (Continued)

		$J=1$–0	$v=1$			$J=1$–0	$v=2$		
IRAS name	$V_{\rm lsr}$	$T_{\rm a}$	S	r.m.s.	$V_{\rm lsr}$	$T_{\rm a}$	S	r.m.s.	Obs. date
	(km s^{-1})	(K)	(K km s^{-1})	(K)	(km s^{-1})	(K)	(K km s^{-1})	(K)	(yymmdd.d)
19291+0502	−5.0	0.942	3.309	0.085	−4.2	1.206	3.555	0.130	010212.5
19303+1553	8.2	0.461	1.868	0.061	9.2	0.485	1.767	0.086	010212.5
19305+2410	22.7	0.546	1.714	0.068	22.6	0.518	2.086	0.094	000417.4
19307+1338	43.5	0.741	2.908	0.048	43.5	0.342	0.857	0.074	010212.5
19309+2022	45.6	0.397	1.260	0.076	45.3	0.898	1.132	0.081	000426.4
19312+1130	65.9	1.905	5.394	0.075	66.3	1.776	4.771	0.094	010215.4
19323+2103	14.0	0.263	0.805	0.041	11.8	0.183	0.479	0.046	000426.4
19333+1918	−23.5	0.300	0.914	0.038	−20.3	0.282	0.686	0.058	010212.5
19344+2114	⋯	⋯	⋯	0.053	44.3	0.476	0.997	0.080	010212.6
19347+2755	26.4	0.113	0.218	0.041	29.5	0.185	0.325	0.046	000422.4
19349+1657	12.5	0.264	1.014	0.040	12.5	0.282	0.840	0.048	000524.2
19352+1914	−12.8	0.500	2.070	0.050	−12.6	0.490	1.866	0.061	000524.3
19361+1805	24.5	0.590	2.108	0.059	23.1	0.422	1.492	0.057	000531.2
19371+2855	23.6	1.220	4.974	0.130	25.0	1.150	3.611	0.174	000421.4
19374+0550	−17.0	3.696	12.452	0.085	−17.5	5.195	15.051	0.126	010213.3
19382+3400	4.7	0.176	0.266	0.051	4.5	0.418	0.812	0.056	000423.4
19386+1513	1.8	0.818	3.485	0.061	0.7	0.743	2.824	0.086	010213.3
19387+1527	59.8	0.370	0.694	0.088	59.9	0.713	0.795	0.103	000529.3
19393+2447	18.8	0.220	1.649	0.031	(18.0)	(0.148)	(0.240)	0.050	010213.3
19395+1827	−0.5	1.160	2.030	0.063	−0.4	0.829	2.583	0.081	010319.5
19395+1949	43.2	1.060	2.939	0.069	42.8	0.843	2.310	0.089	010215.4
19399+2258	−0.3	0.283	1.715	0.049	⋯	⋯	⋯	0.062	000415.4
19405+2938	11.2	0.463	1.584	0.049	10.2	0.386	1.310	0.049	000525.3
19410+2700	−58.8	0.196	1.201	0.033	−60.8	0.184	0.835	0.034	000525.3
19413+2829	26.7	0.240	0.405	0.050	25.7	0.169	0.578	0.052	000427.4
19414+2237	51.8	1.861	6.950	0.132	47.8	0.929	3.883	0.159	000415.4
19422+3506	−50.4	3.115	11.364	0.118	−50.4	3.471	13.080	0.112	000525.4
19425+3323	9.8	5.458	11.280	0.138	9.6	6.255	10.192	0.156	000421.4
19448+2653	1.7	0.529	1.925	0.061	1.1	0.726	2.626	0.074	000529.3
19454+2536	47.4	0.647	3.446	0.051	50.8	1.020	3.593	0.070	010214.3
19459+1716	−1.9	0.236	0.745	0.035	−2.1	0.130	0.653	0.042	000529.3
19459+2815	−59.4	0.293	0.867	0.036	−59.6	0.290	0.677	0.047	000525.2
19462+2232	12.4	0.672	2.243	0.075	12.3	1.102	2.877	0.099	010214.3
19471+2944	−46.5	0.648	2.299	0.036	−40.9	0.454	1.850	0.039	000526.3
19484+1923	85.0	0.851	2.373	0.063	82.8	0.558	2.157	0.079	010319.5
19493+2905	−21.9	2.580	8.931	0.070	−21.8	3.911	13.190	0.093	010214.3
19495+0835	44.5	6.438	16.734	0.098	44.3	7.977	16.065	0.125	010214.4
19499+2141	3.6	0.449	0.973	0.040	2.9	0.292	0.919	0.053	010214.4
19508+2659	6.1	0.555	1.632	0.097	4.7	0.598	1.720	0.102	000427.4
19519+2527	−14.6	0.243	1.527	0.038	−14.4	0.231	0.339	0.052	010214.4

Table 1. (Continued)

		$J=1$–0	$v=1$			$J=1$–0	$v=2$		
IRAS name	$V_{\rm lsr}$	$T_{\rm a}$	S	r.m.s.	$V_{\rm lsr}$	$T_{\rm a}$	S	r.m.s.	Obs. date
	(km s^{-1})	(K)	(K km s^{-1})	(K)	(km s^{-1})	(K)	(K km s^{-1})	(K)	(yymmdd.d)
19522+1935	70.6	0.944	4.796	0.080	65.7	0.715	2.265	0.095	010215.3
19527+2231	39.0	0.675	2.791	0.092	39.5	0.899	1.727	0.111	000524.3
19542+3120	−1.4	0.356	0.965	0.062	−4.7	0.545	2.201	0.076	000524.4
19552+2138	48.6	0.365	1.135	0.046	51.0	0.312	1.196	0.055	000530.3
19583+1323	−24.9	1.072	2.745	0.068	−24.7	0.643	2.266	0.084	000530.3
20005+1635	(−5.0)	(0.135)	(0.143)	0.048	−7.7	0.251	0.475	0.060	000530.3
20010+3011	21.2	1.325	6.778	0.100	21.0	1.891	7.774	0.142	000417.5
20024+1727	−0.6	1.074	2.555	0.148	−3.3	1.626	3.099	0.178	000420.5
20095+2726	12.3	0.430	0.884	0.068	12.4	0.636	1.866	0.095	000417.5
20118+3107	−7.5	0.267	0.430	0.050	−6.4	0.321	0.928	0.058	000522.4
20156+2130	21.2	1.094	5.741	0.066	21.5	0.729	3.590	0.087	010215.3
20171+2732	48.0	0.710	1.814	0.090	48.1	0.616	1.497	0.098	000424.5
20181+2234	40.8	0.739	1.844	0.078	40.4	1.368	2.607	0.091	010215.4
20246+2813	18.1	1.211	4.178	0.145	18.2	1.214	5.260	0.172	000419.5
20280+2631	14.0	0.637	1.069	0.116	15.0	0.699	1.499	0.127	000419.5

Note. The numbers in parentheses are tentative detections.

Table 2. List of non-detections

IRAS name	r.m.s. (J =1–0, v =1)	r.m.s. (J =1–0, v =2)	Obs. date
	(K)	(K)	(yymmdd.d)
18392+1328	0.074	0.052	000415.3
18425+1727	0.057	0.041	000415.3
18462+1208	0.069	0.045	000417.3
18490+1158	0.044	0.030	000417.3
18501+1019	0.091	0.069	000415.4
18512+2029	0.091	0.069	000415.4
18520+1014	0.067	0.050	000417.3
18526+0945	0.060	0.053	000418.3
18554+1333	0.050	0.055	000525.2
18563+2319	0.060	0.062	000526.0
18568+1814	0.056	0.049	000426.3
18578+0951	0.062	0.053	000418.3
18588+1400	0.074	0.065	000419.4
19005+0843	0.072	0.057	000419.3
19007+1652	0.050	0.053	000527.0
19012+1128	0.065	0.052	000418.3
19025+0702	0.075	0.062	000421.3
19026+1300	0.041	0.037	000426.3
19029+0808	0.074	0.050	010212.3
19035+1010	0.068	0.057	000418.3
19039+1733	0.047	0.046	000527.2
19041+1734	0.062	0.054	000422.4
19061+1041	0.057	0.048	000425.3
19099+1145	0.048	0.043	000427.3
19102+1356	0.063	0.063	000527.2
19106+1708	0.060	0.061	000527.2
19112+1439	0.086	0.060	000529.2
19114+0920	0.075	0.066	000424.4
19114+0743	0.060	0.050	000425.3
19131+1551	0.068	0.054	000428.3
19135+0931	0.062	0.057	000420.3
19136+2055	0.080	0.084	000421.4
19140+0652	0.062	0.053	000424.4
19140+1313	0.048	0.052	000530.1
19148+1138	0.080	0.064	000419.4
19159+1744	0.075	0.059	000428.3
19201+1040	0.048	0.051	000530.2
19202+2009	0.070	0.050	000417.4
19206+2121	0.068	0.051	000417.4
19211+1606	0.071	0.049	010212.4

Table 2. (Continued)

IRAS name	r.m.s. (J =1–0, v =1)	r.m.s. (J =1–0, v =2)	Obs. date
	(K)	(K)	(yymmdd.d)
19227+1700	0.070	0.046	010212.4
19236+2003	0.075	0.065	000424.4
19236+2404	0.099	0.079	000421.4
19238+1159	0.059	0.051	000425.4
19244+2015	0.077	0.053	000417.4
19246+1736	0.051	0.057	000529.2
19253+1114	0.043	0.035	000529.2
19263+1810	0.086	0.065	010207.6
19267+0345	0.074	0.050	010212.4
19267+1354	0.050	0.054	000530.2
19268+1904	0.070	0.048	010212.4
19274+1835	0.070	0.047	010212.4
19276+0739	0.084	0.069	000606.9
19276+2158	0.068	0.048	010212.4
19282+2253	0.085	0.061	000603.1
19283+2753	0.061	0.055	000527.3
19285+1808	0.081	0.065	000425.4
19296+2227	0.070	0.049	010212.5
19304+2529	0.073	0.062	000423.4
19315+1807	0.071	0.048	010212.5
19320+2013	0.077	0.049	010212.5
19325+1725	0.067	0.063	000427.4
19325+2346	0.077	0.048	010212.5
19329+2641	0.152	0.121	000420.4
19338+1522	0.050	0.037	010319.4
19339+2408	0.064	0.054	000424.4
19342+2331	0.061	0.049	010319.5
19343+0912	0.078	0.055	010212.6
19344+1921	0.062	0.068	000531.1
19348+2136	0.068	0.044	010213.3
19349+2438	0.070	0.067	000426.4
19351+1922	0.052	0.055	000524.3
19352+2000	0.053	0.060	000524.3
19355+2949	0.069	0.059	000426.4
19360+3442	0.091	0.074	000419.4
19366+2147	0.083	0.058	010212.6
19382+2753	0.083	0.078	000419.4
19394+2959	0.098	0.069	000529.3
19396+1637	0.066	0.043	010213.3
19403+1141	0.050	0.041	010215.4
19410+2800	0.061	0.059	000525.3

Table 2. (Continued)

IRAS name	r.m.s. (J =1–0, v =1) (K)	r.m.s. (J =1–0, v =2) (K)	Obs. date (yymmdd.d)
19411+2400	0.068	0.044	010213.3
19412+2619	0.051	0.055	000530.2
19414+3004	0.063	0.061	000525.3
19415+2832	0.071	0.066	000525.4
19415+2814	0.051	0.045	000527.3
19417+3053	0.095	0.077	000421.4
19417+2930	0.047	0.042	000527.3
19423+1653	0.049	0.063	000530.2
19427+2741	0.082	0.074	000527.4
19427+3034	0.063	0.072	000525.4
19438+0933	0.089	0.078	000428.3
19439+3357	0.052	0.044	000424.4
19450+1556	0.062	0.040	010213.4
19451+3045	0.075	0.066	000426.4
19454+3356	0.071	0.075	000525.4
19457+0832	0.081	0.066	000428.3
19466+1726	0.084	0.062	000417.4
19470+2603	0.041	0.054	010214.3
19485+3235	0.107	0.088	000421.4
19488+1719	0.083	0.063	000529.3
19495+2854	0.062	0.052	000526.3
19500+2239	0.060	0.052	000526.3
19507+3039	0.048	0.040	000428.4
19508+2014	0.063	0.068	000529.3
19509+2930	0.078	0.057	000417.5
19510+1917	0.058	0.066	000529.3
19520+2729	0.056	0.042	010215.3
19524+2957	0.081	0.074	000427.4
19526+2600	0.056	0.046	000428.4
19533+2530	0.053	0.058	000524.3
19534+1757	0.061	0.069	000524.3
19534+2802	0.065	0.060	000526.3
19535+2157	0.039	0.031	000530.2
19537+2850	0.075	0.064	000526.4
19552+3142	0.101	0.085	000421.5
19558+3333	0.109	0.097	000421.5
19563+1725	0.071	0.078	000531.3
19573+3143	0.127	0.102	000415.4
19577+2430	0.137	0.163	000531.3
19579+2926	0.078	0.067	000526.4
19584+2652	0.055	0.042	010215.3

Table 2. (Continued)

IRAS name	r.m.s. (J =1–0, v =1) (K)	r.m.s. (J =1–0, v =2) (K)	Obs. date (yymmdd.d)
19587+2257	0.091	0.064	000417.5
19588+2541	0.030	0.036	000428.4
19591+1817	0.077	0.058	010214.4
19594+2512	0.053	0.058	000530.3
20004+2955	0.083	0.079	000419.5
20005+2931	0.089	0.084	000426.5
20014+2830	0.074	0.060	000428.5
20015+3019	0.081	0.068	000420.4
20046+2954	0.086	0.097	000428.5
20053+2958	0.088	0.078	000420.4
20056+1834	0.052	0.057	000530.3
20084+2750	0.081	0.069	000526.4
20117+1634	0.055	0.044	010215.3
20127+2430	0.051	0.039	010214.4
20180+3015	0.061	0.062	000524.4
20287+2719	0.088	0.080	000427.5

Table 3. MSX counterparts of IRAS sources with large separations.

IRAS name	$F_{12}^{\rm iras}$ Jy	$F_{25}^{\rm iras}$ Jy	MSX name	$F_{12}^{\rm msx}$ Jy	$F_{21}^{\rm msx}$ Jy	Separation. (arcsec)
19102+1356	5.78	5.71	MSX5C_G047.7990+01.7814	7.501	4.900	37
19140+1313	14.27	13.25	MSX5C_G047.6006+00.6186	27.033	21.611	38
19276+0736	6.36	4.03	MSX5C_G044.2837−04.9539	7.250	5.599	29
19348+2136	50.25	33.37	MSX5C_G057.3350+00.3155	49.489	37.488	25
19509+2930	13.92	13.84	MSX5C_G065.9956+01.1562	26.909	29.816	34

Table 4. Results of Confirmation at MSX positions

	$J=1$–0	v=1			$J=1$–0	v=2			
IRAS name	$V_{\rm lsr}$	$T_{\rm a}$	S	r.m.s.	$V_{\rm lsr}$	$T_{\rm a}$	S	r.m.s.	Obs. date
	(km s^{-1})	(K)	(K km s^{-1})	(K)	(km s^{-1})	(K)	(K km s^{-1})	(K)	(yymmdd.d)
19102+1356	52.1	0.580	1.403	0.063	52.6	0.521	0.994	0.082	010319.3
19140+0652	27.3	0.366	0.886	0.041	28.3	0.287	0.844	0.052	010319.3
19276+0739	94.9	0.499	3.040	0.055	93.2	0.801	2.391	0.078	010319.3
19348+2136	34.3	0.134	0.831	0.026	34.8	0.123	0.265	0.035	010319.4
19509+2930	−40.0	2.194	5.043	0.132	−39.5	2.765	5.141	0.165	010523.0

Table 5. IRAS Data.

IRAS name	l	b	F_{12}	C_{12}	C_{23}	D_L	V_{lsr}	OH	H_2O	SiO
	(°)	(°)	(Jy)			(kpc)	(km s^{-1})			
18392+1328	43.95	8.28	8.968	−0.08	−0.82	4.1	⋯			
18413+1354	44.56	8.02	225.100	−0.17	−0.85	0.6	−15.4	y[26]	y[5]	y[7]
18423+1616	46.82	8.85	8.255	−0.17	−0.82	3.3	38.4	n[21]		
18425+1727	47.91	9.32	24.970	−0.19	−0.72	1.8	⋯	n[21]		
18432+1343	44.60	7.51	15.230	−0.13	−0.80	2.7	37.1	n[21]		
18456+1351	44.99	7.05	3.056	−0.14	−0.53	5.9	−17.5	n[21]		
18462+1208	43.52	6.15	8.551	−0.18	−0.98	3.1	⋯	n[4]		
18490+1158	43.67	5.46	9.061	−0.02	−0.73	4.8	⋯	y[17]	n[8]	
18498+1014	42.21	4.50	4.449	−0.20	−0.78	4.0	81.2	n[21]		
18501+1019	42.32	4.47	11.230	0.06	−0.57	5.1	⋯	y[17]	n[8]	
18506+0912	41.38	3.86	8.056	0.02	−0.60	5.6	48.0	y[6]	n[8]	
18511+1141	43.65	4.87	4.288	−0.09	−0.79	5.8	44.9	y[6]	n[8]	
18512+2029	51.60	8.79	36.110	−0.02	−0.80	2.4	⋯	y[17]	y[8]	
18520+1014	42.45	4.02	9.728	−0.01	−0.83	4.7	⋯	y[6]	y[3]	
18526+0945	42.10	3.67	5.808	−0.07	−0.65	5.3	⋯			
18528+1543	47.45	6.35	13.260	−0.09	−0.74	3.3	−17.5			
18530+0817	40.82	2.92	43.750	−0.11	−0.77	1.7	−2.4	n[21]		
18531+1829	49.97	7.51	3.658	−0.15	−0.87	5.2	55.2	n[4]		
18535+0726	40.13	2.42	62.980	0.05	−0.79	2.1	48.9	y[17]	y[3]	n[12]
18545+1040	43.12	3.68	48.200	−0.20	−0.84	1.2	51.9	n[21]		
18547+1254	45.14	4.65	7.993	−0.09	−0.69	4.2	33.0			
18549+0905	41.76	2.86	22.920	−0.09	−0.75	2.5	20.8	y[6]	y[3]	
18554+1333	45.79	4.80	4.667	−0.07	−0.71	5.9	⋯	y[6]	n[8]	
18556+0811	41.04	2.29	103.500	−0.09	−0.92	1.2	37.1	y[6]	y[3]	
18556+1409	46.36	5.01	5.722	−0.09	−0.60	5.0	87.8	y[6]	n[8]	
18563+0816	41.18	2.18	5.345	0.15	−0.55	8.3	13.3	y[6]	n[8]	
18563+2319	54.69	8.97	3.471	−0.16	−0.73	5.2	⋯	n[21]		
18567+1046	43.47	3.24	18.670	−0.10	−0.75	2.7	0.3	y[4]	n[8]	
18568+1814	50.15	6.61	7.676	−0.20	−0.74	3.1	⋯	n[21]		
18578+0951	42.78	2.58	16.900	−0.08	−0.67	3.0	⋯			
18581+1405	46.58	4.45	5.181	−0.11	−0.65	5.0	124.2	y[29]	n[8]	
18585+0900	42.09	2.05	56.840	0.05	−0.64	2.2	78.4	y[6]	n[8]	
18588+1400	46.58	4.28	18.380	0.02	−0.83	3.7	⋯	y[6]	n[8]	
18590+2025	52.35	7.13	4.458	−0.12	−0.63	5.2	70.1	n[4]		
18592+1455	47.45	4.60	37.650	−0.17	−0.76	1.5	0.4		y[8]	
19005+0843	42.06	1.46	17.380	0.08	−0.56	4.2	⋯	n[4]		
19007+1652	49.34	5.16	4.301	−0.07	−0.80	6.1	⋯	y[6]	y[8]	
19008+0907	42.47	1.58	7.610	−0.04	−0.64	5.0	11.5	y[4]	y[8]	
19010+1307	46.03	3.39	7.741	0.16	−0.67	6.9	59.9	y[6]	y[8]	
19012+1128	44.59	2.58	6.920	−0.14	−0.69	3.9	⋯	y[4]	y[8]	
19023+0745	41.42	0.64	11.080	0.16	−0.57	5.8	33.1	y[6]	n[8]	
19024+1923	51.78	5.96	21.670	−0.08	−0.79	2.6	27.3	y[6]	n[8]	
19025+0702	40.80	0.24	20.400	0.09	−0.54	4.0	⋯	n[4]		
19026+1300	46.11	2.99	3.557	0.10	−0.53	9.6	⋯	y[4]	n[8]	
19029+2305	55.16	7.53	6.406	−0.17	−0.69	3.7	−22.4	n[4]		
19029+0808	41.83	0.67	80.550	−0.11	−0.54	1.3	⋯	n[4]		
19029+0933	43.09	1.32	18.180	−0.06	−0.54	3.1	60.0	y[6]	n[8]	
19032+1715	49.96	4.81	17.190	−0.15	−0.77	2.4	−17.4	n[4]		
19035+1010	43.69	1.48	7.560	0.01	−0.55	5.6	⋯	y[4]	n[8]	
19039+1733	50.30	4.80	3.919	−0.17	−0.59	4.7	⋯	n[4]		

Table 5. (Continued)

IRAS name	l (°)	b (°)	F_{12} (Jy)	C_{12}	C_{23}	D_L (kpc)	$V_{\rm lsr}$ (km s^{-1})	OH	H_2O	SiO
19039+1634	49.44	4.35	5.180	−0.10	−0.73	5.1	59.4	n[4]		
19041+0952	43.50	1.21	13.490	0.02	−0.80	4.3	65.4	y[6]	n[8]	
19041+1734	50.35	4.76	6.301	−0.19	−0.72	3.5	···	y[4]	y[8]	
19043+1009	43.78	1.30	54.770	−0.01	−0.71	2.0	46.7	y[17]	y[3]	
19044+0833	42.36	0.54	13.140	0.02	−0.56	4.4	32.4	n[4]		
19047+1539	48.69	3.76	10.590	−0.03	−0.73	4.3	96.6			
19052+0922	43.19	0.74	24.780	−0.12	−0.55	2.2	44.2	y[4]	y[8]	
19061+1041	44.46	1.16	9.484	0.05	−0.63	5.4	···	y[6]	y[3]	
19065+1444	48.09	2.94	4.073	−0.06	−0.90	6.5	5.2			
19068+1127	45.22	1.36	18.150	0.03	−0.76	3.8	9.2	y[6]	y[8]	
19071+0625	40.79	−1.06	15.520	−0.03	−0.81	3.6	91.2			
19079+1143	45.58	1.24	10.410	−0.04	−0.91	4.3	38.6	y[6]	n[8]	
19083+0851	43.08	−0.19	41.600	−0.06	−0.76	2.0	56.8	n[17]	y[8]	
19087+1413	47.88	2.22	9.513	−0.04	−0.74	4.5	36.4	n[4]		
19088+1129	45.47	0.94	15.650	−0.07	−1.02	3.2	33.7	y[6]	y[3]	
19099+1145	45.84	0.83	6.900	−0.11	−0.51	4.3	···	n[21]		
19102+1356	47.79	1.79	5.784	−0.01	−0.73	6.1	···			
19106+1708	50.68	3.18	4.080	−0.16	−0.61	4.8	···	n[21]		
19108+1310	47.18	1.29	5.331	−0.11	−0.53	4.9	54.7	n[21]		
19112+1439	48.55	1.91	4.444	−0.05	−0.52	6.4	···			
19114+0920	43.87	−0.63	9.900	0.00	−0.57	4.8	···	n[21]		
19114+0743	42.43	−1.39	10.610	−0.19	−0.68	2.7	···	n[4]		
19128+1310	47.41	0.87	11.280	0.18	−0.51	5.8	59.7	y[6]	n[8]	
19131+1551	49.81	2.06	25.820	0.06	−0.52	3.4	···	n[4]		
19135+0931	44.27	−0.99	233.700	−0.07	−0.78	0.8	···	n[4]		
19136+2055	54.35	4.32	6.242	0.18	−0.54	7.8	···			
19140+0652	41.98	−2.36	8.376	0.12	−0.61	6.4	···	y[6]	n[8]	
19140+1313	47.59	0.63	14.270	−0.03	−0.60	3.7	···			
19147+1349	48.21	0.77	23.070	−0.06	−0.77	2.7	25.0	y[4,17]	n[8]	
19148+1138	46.30	−0.29	11.210	0.03	−0.73	4.8	···	n[4]		
19149+1638	50.71	2.05	14.480	0.01	−0.68	4.1	43.0	y[4]	n[8]	
19159+1744	51.80	2.36	3.452	0.01	−0.61	8.3	···	n[21]		
19160+0755	43.14	−2.30	7.451	0.12	−0.60	6.8	42.2	y[6]	y[3]	
19161+2343	57.12	5.12	112.200	0.09	−0.65	1.7	24.7	y[26]	y[3]	
19167+1733	51.72	2.09	12.460	−0.07	−0.90	3.6	37.2	y[6]	n[8]	
19175+0958	45.13	−1.65	6.559	0.05	−0.87	6.5	48.1	y[6]	y[8]	
19176+1939	53.68	2.91	8.604	−0.04	−0.59	4.7	54.2	y[27]	n[8]	
19186+1657	51.41	1.42	36.280	−0.09	−0.54	2.0	74.0		n[8]	
19187+2221	56.18	3.95	4.808	−0.16	−0.64	4.4	−13.6		n[8]	
19190+3035	63.55	7.72	5.337	0.13	−0.70	8.1	0.7	y[6]	n[8]	
19190+1128	46.63	−1.28	27.130	0.13	−0.55	3.6	57.9	y[17,6]	n[8]	
19192+0922	44.80	−2.31	127.200	0.09	−0.57	1.6	−70.9	y[4]		y[23]
19195+1747	52.24	1.63	24.240	−0.13	−0.82	2.2	35.3	y[4]	n[8]	
19195+0522	41.31	−4.27	16.160	−0.02	−0.72	3.6	−18.1	y[17]	n[8]	
19201+1040	46.05	−1.88	6.708	0.17	−0.52	7.5	···	y[4]	n[8]	
19202+2009	54.41	2.60	13.620	−0.01	−0.81	4.0	···	n[17]		
19206+2255	56.90	3.83	7.208	−0.14	−0.81	3.8	−34.1	n[21]	y[8]	
19206+2121	55.51	3.08	10.350	−0.11	−0.75	3.5	···	y[4]		
19206+2517	58.98	4.93	5.332	−0.14	−0.83	4.5	33.6	y[6]	n[8]	
19211+1606	50.95	0.49	27.180	−0.11	−0.59	2.2	···	n[4]		

Table 5. (Continued)

IRAS name	l (°)	b (°)	F_{12} (Jy)	C_{12}	C_{23}	D_L (kpc)	$V_{\rm lsr}$ (km s^{-1})	OH	H$_2$O	SiO
19212+1843	53.27	1.70	9.550	−0.19	−0.67	2.8	14.0	n[21]		
19213+0340	40.02	−5.46	13.160	−0.19	−0.84	2.4	23.4	n[21]		
19214+0513	41.40	−4.77	6.905	0.00	−0.59	5.8	10.0	y[6]	y[8]	
19227+1700	51.93	0.58	52.020	0.18	−0.62	2.7	···	n[17]	y[19]	
19229+1708	52.07	0.59	46.080	−0.11	−0.67	1.7	42.0		y[8]	
19231+3555	68.74	9.39	111.900	−0.09	−0.84	1.1	−23.4		n[8]	
19236+2003	54.70	1.85	15.240	−0.09	−0.55	3.1	···	n[4]		
19236+2404	58.24	3.77	7.788	−0.17	−0.74	3.4	···	n[21]		
19236+1359	49.37	−1.06	19.910	0.03	−0.54	3.6	35.2	n[4]		
19237+1430	49.85	−0.83	18.490	0.09	−0.74	4.2	76.8	y[6]	n[8]	
19238+1159	47.64	−2.07	53.030	0.05	−0.50	2.3	···	n[21]		
19240+3615	69.12	9.39	97.390	−0.08	−0.86	1.2	38.0			
19244+1809	53.13	0.78	25.890	−0.12	−0.83	2.2	44.4	n[4]		
19244+2015	54.96	1.78	10.240	0.04	−0.55	5.1	···	n[4]		
19246+1736	52.67	0.47	16.840	0.04	−0.60	4.0	···	n[4]		
19252+2201	56.61	2.47	65.210	−0.14	−0.82	1.3	−19.6	n[21]		
19253+1114	47.16	−2.74	3.936	0.01	−0.81	7.8	···	y[6]	n[8]	
19259+0510	41.87	−5.76	8.931	−0.20	−0.85	2.8	12.1	n[25]	y[8]	
19263+1810	53.36	0.39	17.410	−0.12	−0.58	2.6	···	n[4]		
19264+1132	47.55	−2.83	19.040	−0.15	−0.83	2.3	−29.4	n[4]		
19265+3116	64.91	6.60	7.326	−0.15	−0.74	3.7	35.5	n[11]	y[8]	
19267+0345	40.72	−6.60	44.730	−0.18	−0.90	1.4	···	n[21]		
19267+1354	49.66	−1.75	3.072	−0.17	−0.54	5.3	···	n[4]		
19268+1904	54.21	0.71	13.840	−0.13	−0.52	2.9	···	n[4]		
19270+2239	57.36	2.39	41.260	−0.14	−0.91	1.6	8.8	n[21]		
19271+1354	49.72	−1.85	29.820	−0.18	−0.78	1.7	51.0	y[4]	y[8]	
19274+1835	53.85	0.36	34.450	−0.11	−0.78	1.9	···	n[21]	y[20]	
19276+1500	50.73	−1.41	8.732	−0.02	−0.73	4.9	43.1		y[8]	
19276+0739	44.28	−4.95	6.360	−0.20	−0.58	3.4	···		n[8]	
19276+2158	56.84	1.94	11.230	−0.11	−0.55	3.4	···	n[4]		
19282+2253	57.70	2.28	19.340	−0.08	−0.67	2.8	···	n[4]		
19283+1421	50.25	−1.88	15.200	0.00	−0.78	3.9	−5.0	y[18]		
19283+2753	62.11	4.65	4.028	−0.02	−0.73	7.2	···	n[21]		
19285+1808	53.59	−0.10	41.830	−0.15	−0.59	1.5	···			
19288+2923	63.48	5.28	40.430	0.15	−0.62	3.0	−37.6	y[6]	y[3]	y[23]
19290+1600	51.78	−1.23	8.339	−0.18	−0.54	3.1	55.8	y[4]	n[8]	
19291+0502	42.14	−6.53	23.770	−0.20	−0.77	1.7	−4.59	y[4]	y[8]	
19296+2227	57.48	1.78	31.730	0.12	−0.50	3.3	···	n[21]	y[22]	
19303+1553	51.82	−1.56	10.540	−0.03	−0.83	4.3	8.72	y[6,27]	y[8,3]	
19304+2529	60.23	3.09	37.090	0.13	−0.59	3.1	···	n[21]		
19305+2410	59.08	2.43	22.120	−0.19	−0.79	1.9	22.6	y[4]	y[8]	
19307+1338	49.89	−2.73	83.070	−0.10	−0.87	1.3	43.5	n[21]	y[20]	
19309+2022	55.81	0.50	13.130	−0.18	−0.90	2.5	45.5	n[4]		
19312+1130	48.09	−3.87	9.948	−0.12	−0.77	3.5	66.1	y[4,27,25]	y[8]	
19315+1807	53.91	−0.72	16.720	−0.08	−0.52	3.0	···	n[4]		
19320+2013	55.80	0.20	14.040	−0.04	−0.72	3.7	···	n[4]		
19323+2103	56.56	0.56	10.540	−0.10	−0.57	3.6	12.9	n[4]		
19325+1725	53.42	−1.26	13.750	0.10	−0.59	4.9	···			
19325+2346	58.96	1.83	44.050	−0.13	−0.63	1.6	···	n[21]	y[20]	
19329+2641	61.55	3.19	55.900	−0.19	−0.89	1.2	···	n[21]		

Table 5. (Continued)

IRAS name	l	b	F_{12}	C_{12}	C_{23}	D_L	$V_{\rm lsr}$	OH	H_2O	SiO
	(°)	(°)	(Jy)			(kpc)	(km s^{-1})			
19333+1918	55.15	−0.51	24.590	−0.07	−0.64	2.6	−21.9	y^{4,17}	y^{8}	
19338+1522	51.78	−2.56	8.718	−0.17	−0.92	3.2	⋯	n^{30}		
19339+2408	59.43	1.74	5.242	−0.06	−0.75	5.7	⋯	n^{21}		
19342+2331	58.93	1.37	7.350	−0.19	−1.05	3.2	⋯	n^{4}		
19343+0912	46.44	−5.67	10.200	−0.10	−0.78	3.6	⋯	y^{27}	n^{8}	
19344+1921	55.32	−0.71	10.350	−0.17	−0.60	2.9	⋯	n^{4}		
19344+2114	56.96	0.21	7.179	−0.01	−0.64	5.5	44.3			
19347+2755	62.81	3.44	8.859	0.09	−0.77	6.0	27.9	y^{6}	n^{8}	
19348+2136	57.33	0.32	50.250	−0.18	−0.78	1.3	⋯	n^{21}		
19349+2438	59.98	1.79	5.158	−0.16	−0.78	4.3	⋯	n^{21}		
19349+1657	53.29	−2.01	10.570	−0.06	−0.90	4.0	12.5			
19351+1922	55.41	−0.85	14.950	−0.09	−0.68	3.1	⋯	n^{4}		
19352+1914	55.31	−0.94	11.750	−0.03	−0.69	4.1	−12.7	y^{4}	y^{8}	
19352+2000	55.98	−0.57	12.650	−0.13	−0.68	3.0	⋯	n^{4}		
19355+2949	64.57	4.20	5.264	−0.19	−0.66	3.8	⋯	n^{21}		
19360+3442	68.91	6.50	7.043	0.18	−0.65	7.4	⋯	y^{6}	n^{8}	
19361+1805	54.42	−1.68	3.237	−0.05	−0.53	7.4	23.8	n^{4}		
19366+2147	57.69	0.04	14.120	−0.18	−0.55	2.4	⋯	n^{4}		
19371+2855	63.95	3.48	50.390	−0.11	−0.81	1.6	24.3	y^{4}	y^{8}	
19374+0550	43.85	−7.95	155.200	−0.13	−0.87	0.9	−17.2	n^{21}	y^{31}	n^{13}
19382+2753	63.17	2.75	10.220	−0.17	−0.62	2.9	⋯	n^{4}		
19382+3400	68.51	5.76	7.517	−0.08	−0.86	4.5	4.6	y^{21}		
19386+1513	52.22	−3.63	38.160	−0.06	−0.87	2.1	1.24	y^{6}	y^{8,12,3,28,10}	y^{12}
19387+1527	52.44	−3.54	6.479	0.08	−0.73	6.9	59.8	y^{6}	y^{8}	n^{12}
19393+2447	60.61	0.99	12.940	−0.10	−0.66	3.2	18.4	n^{4,11,25}		
19394+2959	65.14	3.56	6.008	0.05	−0.61	6.8	⋯	n^{21}		
19395+1827	55.13	−2.20	8.346	−0.09	−0.64	4.1	−0.5	n^{29}	n^{8}	
19395+1949	56.32	−1.52	9.834	−0.07	−0.67	4.0	43.0	y^{21}	n^{8}	
19396+1637	53.57	−3.15	119.100	−0.16	−0.94	0.9	⋯	n^{21,24}	n^{24}	n^{1}
19399+2258	59.10	−0.02	16.980	−0.08	−0.57	3.0	−0.3	n^{4}		
19403+1141	49.34	−5.73	8.903	−0.12	−1.00	3.7	⋯	n^{21}		
19405+2938	64.94	3.18	3.195	−0.17	−0.61	5.2	10.7	n^{4}		
19410+2700	62.72	1.77	3.571	−0.08	−0.64	6.5	−59.8	n^{4}		
19410+2800	63.59	2.27	5.082	−0.20	−0.59	3.8	⋯	n^{4}		
19411+2400	60.13	0.25	15.440	−0.17	−0.53	2.4	⋯	n^{4,11}		
19412+2619	62.15	1.39	6.760	0.10	−0.72	7.0	⋯			
19413+2829	64.04	2.45	4.257	0.05	−0.69	8.1	26.2	y^{21}	n^{8}	
19414+2237	58.97	−0.50	21.210	−0.18	−0.89	2.0	49.8	y^{6}	n^{8}	
19414+3004	65.43	3.23	3.134	−0.14	−0.61	5.8	⋯	n^{4}		
19415+2832	64.09	2.45	3.172	−0.14	−0.54	5.8	⋯	n^{4}		
19415+2814	63.84	2.30	3.753	−0.13	−0.59	5.5	⋯	n^{21}		
19417+3053	66.15	3.58	25.430	−0.11	−0.70	2.2	⋯	n^{4}		
19417+2930	64.96	2.89	3.011	−0.13	−0.53	6.1	⋯	n^{4}		
19422+3506	69.89	5.59	202.900	−0.07	−0.78	0.9	−50.4	y^{21}	y^{8}	
19423+1653	54.12	−3.57	11.500	−0.19	−0.78	2.6	⋯	n^{4}		
19425+3323	68.42	4.67	30.640	−0.19	−0.91	1.6	9.7	y^{4}	y^{8}	
19427+2741	63.49	1.79	4.146	−0.19	−0.68	4.3	⋯	n^{21}		
19427+3034	66.00	3.24	14.060	−0.20	−0.77	2.3	⋯	n^{4}		
19438+0933	47.91	−7.53	19.330	0.00	−0.60	3.4	⋯			
19439+3357	69.05	4.72	8.829	−0.19	−0.89	2.9	⋯	n^{21}		

Table 5. (Continued)

IRAS name	l (°)	b (°)	F_{12} (Jy)	C_{12}	C_{23}	D_L (kpc)	$V_{\rm lsr}$ (km s^{-1})	OH	H_2O	SiO
19448+2653	63.04	0.98	8.794	0.04	−0.59	5.5	1.4	y[21]	n[8]	
19450+1556	53.62	−4.61	21.190	−0.17	−0.75	2.0	⋯	n[4]		
19451+3045	66.42	2.88	11.880	−0.15	−0.62	2.9	⋯	n[4]		
19454+2536	62.00	0.21	16.480	−0.12	−0.65	2.7	49.1	y[4]	y[8]	
19454+3356	69.19	4.44	3.251	−0.16	−0.62	5.4	⋯	n[4]		
19457+0832	47.24	−8.45	16.180	0.06	−0.68	4.2	⋯			
19459+1716	54.88	−4.11	5.755	0.06	−0.68	7.1	−2.0	y[6]	n[8]	
19459+2815	64.35	1.46	4.299	−0.13	−0.63	5.1	−59.5	n[21]		
19462+2232	59.46	−1.51	18.870	−0.06	−0.75	3.0	12.3	y[11,17,6]	y[8,3]	
19466+1726	55.11	−4.18	3.926	−0.18	−0.81	4.6	⋯	n[21]		
19470+2603	62.58	0.13	10.930	−0.19	−0.57	2.7	⋯	n[4]		
19471+2944	65.77	1.99	8.046	−0.03	−0.77	5.0	−43.7	y[21]	y[8]	
19484+1923	57.00	−3.55	7.062	−0.15	−0.91	3.7	82.8	n[21]		
19485+3235	68.37	3.20	29.960	−0.15	−0.73	1.8	⋯	n[4]		
19488+1719	55.27	−4.70	4.200	0.05	−0.70	8.2	⋯	y[6]	n[8]	
19493+2905	65.44	1.25	22.340	0.19	−0.76	4.2	−21.8	y[17,6,27]	y[8,12,9,28]	y[12,15,14]
19495+2854	65.31	1.13	3.066	−0.08	−0.74	7.0	⋯	n[21]		
19495+0835	47.75	−9.24	80.020	−0.09	−0.75	1.3	44.4	y[6]	y[8,3]	
19499+2141	59.17	−2.68	10.390	−0.02	−0.71	4.5	3.3	y[11,17,6]	y[8,3]	
19500+2239	60.01	−2.20	6.476	0.00	−0.75	5.9	⋯	y[6]	n[8]	
19507+3039	66.95	1.80	3.095	0.02	−0.54	9.0	⋯	n[21]		
19508+2014	58.03	−3.60	5.141	0.09	−0.84	7.9	⋯	y[6]	n[8]	
19508+2659	63.83	−0.12	28.120	0.02	−0.71	3.0	5.4	y[17]	y[3]	
19509+2930	65.99	1.16	13.920	0.00	−0.70	4.1	⋯			
19510+1917	57.24	−4.14	3.851	0.01	−0.55	7.9	⋯	n[4]		
19519+2527	62.63	−1.13	13.220	−0.09	−0.60	3.3	−14.5	y[11]	y[20]	
19520+2729	64.38	−0.10	17.970	0.18	−0.64	4.6	⋯	y[6]	y[2]	
19522+1935	57.65	−4.22	29.300	−0.05	−0.74	2.5	68.2	y[6]	y[8,3]	
19524+2957	66.54	1.11	15.030	−0.12	−0.77	2.8	⋯	n[4]		
19526+2600	63.19	−0.98	4.248	0.08	−0.51	8.5	⋯	n[21]		
19527+2231	60.22	−2.80	3.075	−0.09	−0.73	6.8	39.3	y[6]	n[8]	
19533+2530	62.84	−1.37	7.376	0.01	−0.54	5.7	⋯	n[21]		
19534+1757	56.38	−5.30	5.293	0.10	−0.54	7.9	⋯			
19534+2802	65.02	−0.06	8.530	0.14	−0.59	6.5	⋯	y[6]	n[8]	n[12]
19535+2157	59.83	−3.25	3.323	−0.17	−0.75	5.1	⋯	y[4]	y[8]	
19537+2850	65.74	0.30	15.240	−0.07	−0.69	3.2	⋯	n[4]		
19542+3120	67.92	1.51	3.748	−0.13	−0.64	5.5	−3.1	n[21]		
19552+3142	68.34	1.52	35.030	−0.20	−0.67	1.4	⋯	n[4]		
19552+2138	59.77	−3.75	7.158	−0.16	−0.80	3.6	49.8	n[21]		
19558+3333	69.98	2.38	42.940	0.03	−0.57	2.5	⋯	n[17]		
19563+1725	56.29	−6.16	6.415	−0.15	−0.71	3.9	⋯	n[21]		
19573+3143	68.59	1.16	19.100	−0.05	−0.68	3.1	⋯	n[4]		
19577+2430	62.51	−2.74	7.445	−0.17	−0.68	3.4	⋯	n[4]		
19579+2926	66.71	−0.16	5.602	−0.18	−0.79	3.8	⋯	y[4]	y[8]	
19583+1323	53.05	−8.67	14.200	−0.19	−0.87	2.3	−24.8	n[4]		
19584+2652	64.60	−1.62	14.270	−0.01	−0.55	3.9	⋯	n[4,11,17]	n[19]	
19587+2257	61.32	−3.76	3.234	−0.14	−0.78	5.7	⋯	n[4]		
19588+2541	63.64	−2.32	3.469	0.04	−0.53	8.8	⋯	y[4]	n[8]	
19591+1817	57.38	−6.29	40.260	−0.12	−0.80	1.7	⋯	n[4,25]		
19594+2512	63.30	−2.69	3.756	0.05	−0.74	8.6	⋯	n[4]		

Table 5. (Continued)

IRAS name	l (°)	b (°)	F_{12} (Jy)	C_{12}	C_{23}	D_L (kpc)	$V_{\rm lsr}$ (km s^{-1})	OH	H_2O	SiO
20004+2955	67.43	−0.36	31.720	0.07	−0.90	3.1	···			
20005+2931	67.09	−0.60	10.730	−0.13	−0.77	3.2	···	n^{4}		n^{16}
20005+1635	56.10	−7.47	5.534	−0.12	−0.71	4.7	−6.4	n^{4}		
20010+3011	67.72	−0.34	58.180	−0.15	−0.68	1.3	21.1	n^{4}		
20014+2830	66.33	−1.31	24.070	−0.15	−0.53	2.0	···	n^{4}		
20015+3019	67.90	−0.37	162.200	−0.14	−0.65	0.8	···	y^{4}	y^{8}	
20024+1727	57.08	−7.39	60.990	0.00	−0.81	1.9	−1.9	y^{6}	y^{8}	
20046+2954	67.90	−1.15	11.470	−0.20	−0.73	2.5	···	n^{4}		
20053+2958	68.03	−1.23	11.500	−0.10	−0.65	3.4	···	n^{4}		n^{16}
20056+1834	58.44	−7.46	17.520	0.01	−0.52	3.7	···	n^{17}		
20084+2750	66.62	−2.98	9.734	−0.09	−0.71	3.8	···			y^{16}
20095+2726	66.42	−3.38	28.830	−0.04	−0.71	2.6	12.4	y^{17}	n^{8}	
20117+1634	57.53	−9.75	10.600	−0.15	−0.55	3.1	···	n^{21}		
20118+3107	69.77	−1.77	5.258	−0.11	−0.59	4.9	−6.9	n^{21}		
20127+2430	64.36	−5.62	17.400	−0.05	−0.87	3.2	···	y^{4,11,6}	n^{8}	
20156+2130	62.21	−7.82	20.360	−0.13	−0.67	2.4	21.4	n^{11,25}	n^{8}	
20171+2732	67.44	−4.73	15.370	−0.03	−0.64	3.6	48.0	y^{17}	y^{3}	
20180+3015	69.80	−3.36	4.125	−0.17	−0.66	4.6	···	n^{4}		
20181+2234	63.44	−7.72	25.620	0.11	−0.69	3.6	40.6	y^{17,6}	y^{28}	n^{12}
20246+2813	68.97	−5.71	13.560	−0.07	−0.85	3.4	18.1	y^{6}	y^{3}	y^{16}
20280+2631	68.00	−7.30	17.000	0.06	−0.80	4.1	14.5	y^{17}	y^{8}	
20287+2719	68.74	−6.97	7.199	−0.14	−0.81	3.8	···	n^{21}		

References. — 1. Allen et al. (1989); 2. Benson, Little-Marenin (1996); 3. Cesaroni et al. (1988); 4. Chengalur et al. (1993); 5. Comoretto et al. (1990); 6. Eder et al. (1988); 7. Engels, Heske (1989); 8. Engels, Lewis (1996); 9. Engels et al. (1986); 10. Engels et al. (1988); 11. Galt et al. (1989); 12. Gomez et al. (1990); 13. Hall et al. (1990); 14. Jewell et al. (1991); 15. Jewell et al. (1985); 16. Jiang et al. (1999); 17. Le Squeren et al. (1992); 18. Lewis (1994); 19. Lewis, Engels (1993); 20. Lewis, Engels (1995); 21. Lewis et al. (1990); 22. Marvel, Boboltz (1999); 23. Nyman et al. (1998); 24. Seaquist et al. (1995); 25. Sivagnanam et al. (1990); 26. Slootmaker et al. (1985); 27. te Lintel Hekkert et al. (1991); 28. te Lintel Hekkert et al. (1989); 29. Lewis (1997); 30. Lewis et al. (1987) 31. Takaba et al. (2000)

References

Allen, D. A., Hall, P. J., Norris, R. P., Troup, E. R., Wark, R. M., & Wright, A. E. 1989, MNRAS, 236, 363

Anglada, G., Estalella, R., Pastor, J., Rodríguez, L. F., & Haschick, A. D. 1996, ApJ, 463, 205

Beichman, C. A., Neugebauer, G., Habing, H. J., Clegg, P. E., & Chester, T. J. 1988, IRAS Catalogs & Atlases, I. Explanatory Supplement, NASA RP-1190 (US Goverment Printing Office, Washinton) pVII-22

Benson, P. J., & Little-Marenin, I. R. 1996, ApJS, 106, 579

Blommaert , J. A. D. L., van Langevelde, H. J., & Michiels, W. F. P. 1994, A&A, 287, 479

Cesaroni, R., Palagi, F., Felli, M., Catarzi, M., Comoretto, G., di Franco, S., Giovanardi, C., & Palla, F. 1988, A&AS, 76, 445

Chakravarti, I. M., Laha, R. G., & Roy, J. 1967, Handbook of methods of applied statistics (Wiley, New York), p.392

Chengalur, J. N., Lewis, B. M., Eder, J., & Terzian, Y. 1993, ApJS, 89, 189

Comoretto, G., Plagi, f., Cesaroni, R., Felli, M., Bettarini, A., Catarzi, M., Curioni, G. P., Curioni, P. et al. 1990, A&AS, 84, 179

Dame, T. M., Ungerechts, H., Cohen, R. S., de Geus, E. J., Grenier, I. A., May, J., Murphy, D. C., Nyman, L. -Å. & Thaddeus, P. 1987, ApJ, 322, 706

David, P., Le Squeren, A. M., & Sivagnanam, P. 1993, A&A, 277, 453

Deguchi, S., Fujii, T., Izumiura, H., Kameya, O., Nakada, Y., & Nakashima, J. 2000a, ApJS, 130, 351

Deguchi, S., Fujii, T., Izumiura, H., Kameya, O., Nakada, Y., Nakashima, J., Ootsubo, T., & Ukita, N. 2000b, ApJS, 128, 571

Deguchi, S., Fujii, T., Matsumoto, S., Nakashima, J., & Wood, P. R. 2001, PASJ, 54, 719

Dehnen, W., & Binney, J. J. 1998, MNRAS, 298, 387

Eder, J., Lewis, B. M., & Terzian, Y. 1988, ApJS, 66, 183

Engels, D., & Heske, A. 1989, A&AS, 81, 323

Engels, D., & Lewis, B. M. 1996, A&AS, 116, 117

Engels, D., Schmid-Burgk, J., & Walmsley, C. M. 1986, A&A, 167, 129

Engels, D., Schmid-Burgk, J., & Walmsley, C. M. 1988, A&A, 191, 283

Frink, S., Fuchs, B., Roeser, S., & Wielen, R. 1996, A&A, 314, 430

Galt, J. A., Kwok, S., & Frankow, J. 1989, AJ, 98, 2182

Georgelin, Y. M., Georgelin, Y. P., & Sivan, J. P. 1976, A&A, 49, 57

Gomez, Y., Moran, J. M., & Rodriguez, L. F. 1990, Rev. Mex. Astron. Astrofis., 20, 55

Groenewegen, M. A. T., de Jong, T., & Geballe, T. R. 1994, A&A, 287, 163

Groenewegen, M. A. T., & de Jong, T. 1993, A&A, 267, 410

Groenewegen, M. A. T., & de Jong, T. 1998, A&A, 337, 797

Habing, H. J. 1996, A&A Rev., 7, 97

Hall, P. J., Wright, A. E., Troup, E. R., Wark, R. M., & Allen, D. A. 1990, MNRAS, 247, 549

Heske, A., Forveille, T., Omont, A., van der Veen, W. E. C J., & Habing, H. J. 1990, A&A, 239, 173

Honma, M., Oyama, T., Hachisuka, K., Sawada-Satoh, S., Sebata, K., Miyoshi, M., Kameya, O., Manabe, S. et al. 2000, PASJ, 52, 631

Honma, M., & Sofue, Y. 1997, PASJ, 49, 453

Iben, I., Jr. & Renzini, A. 1983, ARA&A, 21, 271

Imai, H., Deguchi, S., Fujii, T., Glass, I. S., Ita, Y., Izumiura, H., Kameya, O., Miyazaki, A., Nakada, Y., & Nakashima, J. 2002, PASJ, 54, L19

Ita, Y., Deguchi, S., Fujii, T., Kameya, O., Miyoshi, M., Nakada, Y., Nakashima, J., & Parthasarathy, M. 2001, A&A, 376, 112

Izumiura, H., Catchpole, R., Deguchi, S., Hashimoto, O., Nakada, Y., Onaka, T., Ono, T., Sekiguchi, K., Ukita, N., & Yamamura, I. 1995a, ApJS, 98, 271

Izumiura, H., Deguchi, S., Fujii, T., Kameya, O., Matsumoto, S., Nakada, Y., Ootsubo, T., & Ukita, N. 1999, ApJS, 125, 257

Izumiura, H., Deguchi, S., Hashimoto, O., Nakada, Y., Onaka, T., Ono, T., Ukita, N., & Yamamura, I. 1994, ApJ, 437, 419

Izumiura, H., Deguchi, S., Hashimoto, O., Nakada, Y., Onaka, T., Ono, T., Ukita, N., & Yamamura, I. 1995b, ApJ, 453, 837

Jewell, P. R., Snyder, L. E., Walmsley, C. M., Wilson, T. L., & Gensheimer, P. D. 1991, A&A, 242, 211

Jewell, P. R., Walmsley, C. M., Wilson, T. L., & Snyder, L. E. 1985, ApJ, 298, L55

Jiang, B. W., Deguchi, S., Hu, J. Y., Yamashita, T., Nishihara, E., Matsumoto, S., & Nakada, Y. 1997, AJ, 113, 1315

Jiang, B. W., Deguchi, S., Izumiura, H., Nakada, Y., & Yamamura, I., 1995, PASJ, 47, 815

Jiang, B. W., Deguchi, S., Ramesh, R. 1999, PASJ, 51, 95

Jiang, B. W., Deguchi, S., Yamamura, I., Nakada, Y., Cho, S. H., & Yamagata, T. 1996, ApJS, 106, 463

Jiang, B. W. & Hu, J. Y. 1993, Chin. Astro. Astrophy., 17, 321

Jura, M., & Kleinmann, S. G. 1989, ApJ, 341, 359

Jura, M., & Kleinmann, S. G. 1990, ApJ, 364, 663

Kerr, F. J., & Lynden-Bell, D. 1986, MNRAS, 221, 1023

Le Squeren, A. M., Sivagnanam, P., Dennefeld, M., & David, P. 1992, A&A, 254, 133

Lewis, B. M. 1994, ApJS, 93, 549

Lewis, B. M. 1997, ApJS, 109, 489

Lewis, B. M., Eder, J., & Terzian, Y. 1987, AJ, 94, 1025

Lewis, B. M., & Engels, D. 1993, MNRAS, 265, 161

Lewis, B. M., & Engels, D. 1995, MNRAS, 274, 439

Lewis, B. M., Eder, J., & Terzian, Y. 1990, ApJ, 362, 634

Lindqvist, M., Habing, H, J., & Winnberg, A. 1992, A&A, 259, 118

Evans, T. L., & Little-Marenin, I. R. 1999, MNRAS, 304, 421

Loup, C., Forveille, T., Omont, A., & Paul, J. F. 1993, A&AS, 99, 291

Margulis, M., van Blerkom, D. J., Snell, R. L., & Kleinmann, S. G. 1990, ApJ, 361, 637

Marvel, K. B., & Boboltz, D. A., 1999, AJ, 118, 1791

Menzies, J. W., & Whitelock, P. A. 1988, MNRAS, 233, 697

Meixner, M., Ueta, T., Dayal, A., Hora, J. L, Fazio, G., Hrivnak, B. J., Skinner, C. J., Hoffmann, W. F. & Deutsch, L. K. 1999, ApJ, 122, 221

Merrifield, M. R. 1992, AJ, 103, 1552

Mihalas, D., & Binney, J., 1981, Galactic Astronomy, (San Francisco: Freeman & Company)

Miyazaki, A., Deguchi, S., Tsuboi, M., Kasuga, T., & Takano, S. 2001, PASJ, 53, 501

Nakashima, J., Deguchi, S., Fujii, T., Izumiura, H., Kameya, O., & Nakada, Y. 2002, ApJ,(submitted to ApJ)

Nakashima, J., Jiang, B. W., Deguchi, S., Sadakane, K., & Nakada, Y. 2000, PASJ, 52, 275

Nyman, L.-Å., Hall, P. J., & Olofsson, H. 1998, A&AS, 127, 185

Olnon, F. M., Raimond, E., & the IRAS Science Team, 1986, A&AS, 65, 607

Price, S. D., Egan, M. P., Shipman, R. F., Tedesco, E. F., Cohen, M., Walker, R. G., & Moshir, M. 1997, BAAS, 29, 1294

Seaquist, E. R., & Ivison, R. J. 1994, MNRAS, 269, 512

Seaquist, E. R., Ivison, R. J., & Hall, P. J., 1995, MNRAS, 276, 867

Sevenster, M. N., Chapman, J. M., Habing, H. J., Killeen, N. E. B., & Lindqvist, M. 1997, A&AS, 122,79

Sivagnanam, P., Braz, M. A., Le Squeren, A. M., & Tran Minh, F. 1990, A&A, 233, 112

Slootmaker, A., Herman, J., & Habing, H. J. 1985, A&AS, 59, 465

Stephenson, C. B. 1990, AJ, 100, 569

Takaba, H., Iwata, T., Miyaji, T., & Deguchi, S. 2000, PASJ, 53, 517

Taylor, J. H.@& Cordes, J. M. 1993, ApJ, 411, 674

te Lintel Hekkert, P., Caswell, J. L., Habing, H. J., Haynes, R. F., & Norris, R. P. 1991, A&AS, 90, 327

te Lintel Hekkert, P., Versteege-Hansel, H. A., Habing, H. J., & Wiertz, M. 1989, A&AS, 78, 399

van der Veen, W. E. C. J., & Breukers, R. J. L. H. 1989, A&A, 212, 133

van der Veen, W. E. C. J., & Habing, H. J. 1988, A&A, 194, 125

van der Veen, W. E. C. J., & Habing, H. J. 1990, A&A, 231, 404

van Langevelde, H. J., van der Heiden, R., & van Schooneveld, C. 1990, A&A, 239, 193

Ventura, P., D'Antona, F., & Mazzitelli, I. 1999, ApJ, 524, L111

Volk, K., Kwok, S., & Langill, P. P. 1992, ApJ, 391, 285

Vassiliadis, E., & Wood, P. R. 1993, ApJ, 413, 641

Walker, H. J., Tsikoudi, V., Clayton, C. A., Geballe, T., Wooden, D. H., & Butner, H. M. 1997, A&A, 323, 442

Wood, P. R., Bessell, M. S., & Fox, M. W. 1983, ApJ, 272, 99

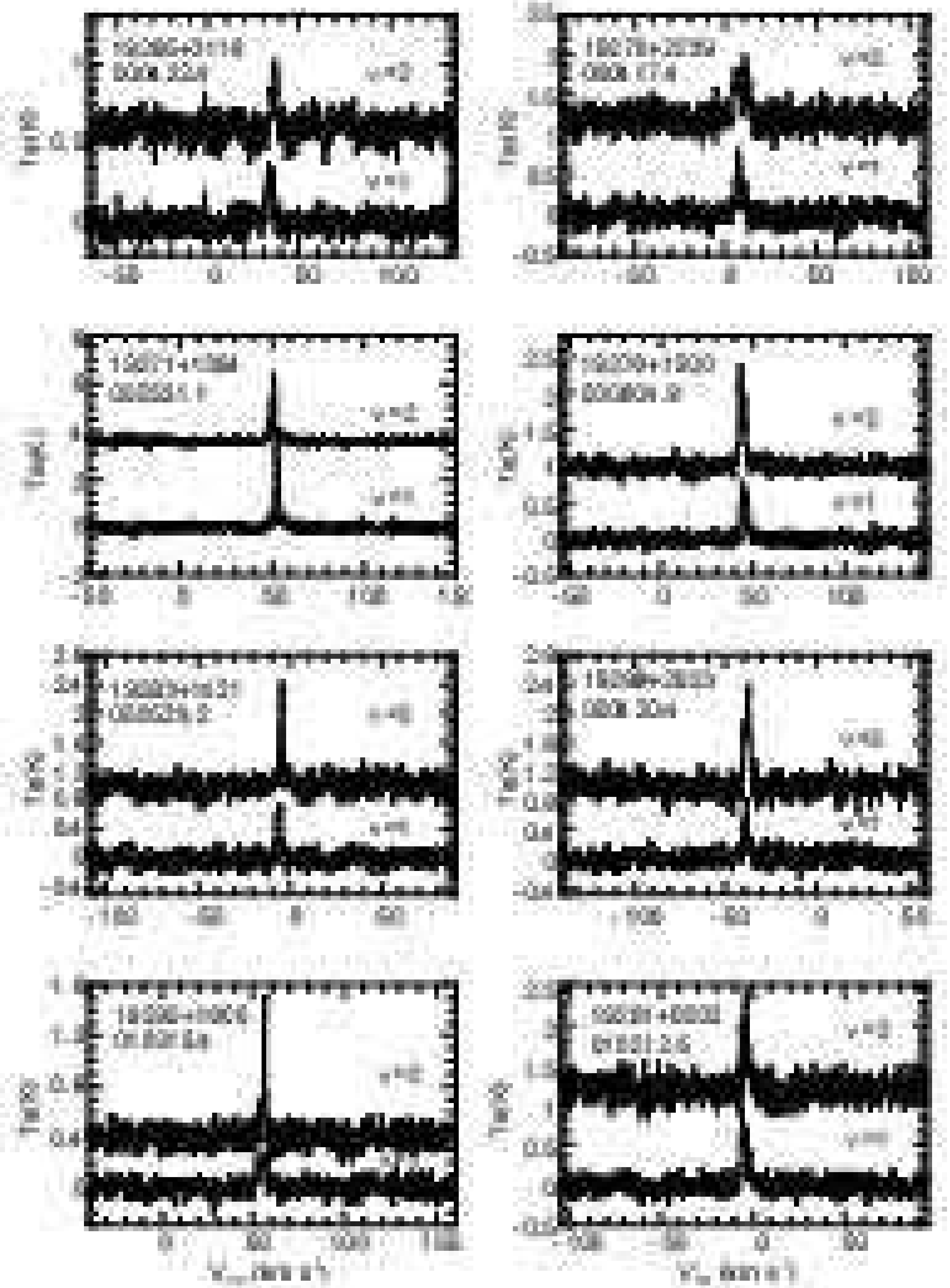

v=2
v=1
T_MB (K)
V_LSR (km s^-1)
-50
0
50
100
150
-100
-50
0
50